JGR Space Physics

RESEARCH ARTICLE
10.1029/2021JA029313

Special Section:
Cluster 20th Anniversary: Results from the First 3D Mission

Results of the Electron Drift Instrument on Cluster

G. Paschmann[1], J. M. Quinn[2], R. B. Torbert[3], C. E. McIlwain[4], H. Vaith[3], S. Haaland[5,6,7], H. Matsui[3], C. A. Kletzing[8], W. Baumjohann[9], and G. Haerendel[1]

[1]Max-Planck-Institut für extraterrestrische Physik, Garching, Germany, [2]Albuquerque, NM, USA, [3]University of New Hampshire, Durham, NH, USA, [4]University of California at San Diego, La Jolla, CA, USA, [5]Max-Planck-Institut für Sonnensystemforschung, Göttingen, Germany, [6]Birkeland Centre for Space Science, University of Bergen, Norway, [7]The University Centre in Svalbard, Longyearbyen, Norway, [8]University of Iowa, Iowa City, IA, USA, [9]Space Research Institute, Austrian Academy of Sciences, Graz, Austria

Abstract The electron drift instrument (EDI) on Cluster pioneered a new method of measuring electric fields, using a beam of electrons to sample the drift velocity over a km-scale gyro orbit. The technique is especially well suited to measuring weak, sub-mV/m, convection fields due to its sensitivity (to both components in the plane perpendicular to *B*) and because it is unaffected by the anomalous local electric fields that are generated by spacecraft-plasma interactions. Because EDI requires exquisite beam pointing with active tracking of the firing directions, measurements are less regular, or even impossible, in rapidly varying electric and magnetic fields; however, in the many regimes where tracking is successful the resulting measurements are reliably accurate. We review the EDI technique and instrumentation, and present six areas of investigation using Cluster data: (1) Detailed comparisons of EDI data with the electric field and waves double probe measurements show excellent agreement in many cases but identify large discrepancies where strong ion outflow in the polar regions creates local spacecraft wake effects. (2) The wake effect is exploited to infer quantitative ion outflow rates. Detailed convection patterns in the (3) polar cap, (4) lobe, and (5) inner magnetosphere are derived under various driver conditions using statistical analyses of long term measurements during the Cluster mission. (6) EDI's large geometric-factor detector is used for extremely high time resolution measurements of electrons at a specified energy and pitch angle.

Key Points:

- Complementarity of electron drift and double-probe techniques established
- Inner magnetosphere, polar cap, and tail-lobe convection patterns determined
- Key contribution to ion outflow velocities made

Correspondence to:
G. Paschmann,
goetz.paschmann@mpe.mpg.de

Citation:
Paschmann, G., Quinn, J. M., Torbert, R. B., McIlwain, C. E., Vaith, H., Haaland, S., et al. (2021). Results of the electron drift instrument on cluster. *Journal of Geophysical Research: Space Physics*, *126*, e2021JA029313. https://doi.org/10.1029/2021JA029313

Received 7 MAR 2021
Accepted 27 MAY 2021

1. Introduction

The electric field is a fundamental quantity in space plasmas, yet it is one of the most difficult to measure. This is because in many situations the electric field is very small (<1 mV/m), and the plasma is very dilute (<1 cm^{-3}), conditions under which it is challenging for the conventional double-probe technique to distinguish natural fields from those induced by spacecraft wakes, photoelectrons, and sheaths. The motivation for the technique implemented with the electron drift instrument (EDI) was to minimize the effects of such spacecraft-perturbed environments, and to measure the full drift velocity vector in the plane perpendicular to the magnetic fields, regardless of the orientation of the spacecraft spin axis. The EDI technique involves sensing the drift of a weak beam of test electrons emitted by electron guns mounted on the spacecraft. When emitted in uniquely defined directions perpendicular to the magnetic field, these electrons return to associated detectors after one or more gyrations in the ambient magnetic field, as proven on the European Space Agency's (ESA's) Geos spacecraft by Melzner et al. (1978).

Although conceptually simple, a practical implementation of the EDI technique must address several challenges that are imposed by the ambient environment. First, for the Cluster mission, the electric and magnetic fields can lie in any orientation with respect to the spacecraft body axes. This means that each electron gun must be able to fire beams in any direction within, at least, a 2π steradian hemisphere. Similarly, each detector must be capable of receiving the return beam over at least a full hemisphere. This constraint means that each detector will, on average, have the sun in its field of view half the time, necessitating an excellent rejection of any background signal from solar ultraviolet (UV), while simultaneously maintaining hemispherical sensitivity to electrons. There were no existing electron guns nor detectors meeting those requirements when EDI development began.

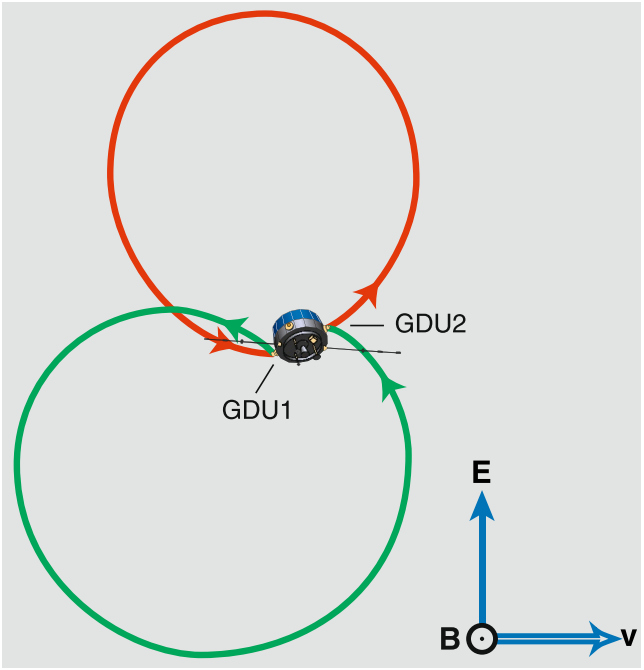

Figure 1. Electron drift instrument principle of operation. For arbitrary combinations of magnetic field $\boldsymbol{B}$ and electric field $\boldsymbol{E}$ (or equivalent drift velocity $\boldsymbol{V}_d$), only one single-gyration electron-trajectory exists that connects each gun with the detector on the opposite side of the spacecraft. The two trajectories differ in their lengths and thus in their times-of-flight. Note that to fit the spacecraft and the electron orbits on the same sale, they are drawn for very high values of drift velocity and magnetic field. From Paschmann et al. (2001).

A second set of challenges flow from the dynamics of the electric and magnetic fields. As these fields vary, acquisition and tracking of the needed firing direction (that for which the beam returns to the spacecraft) requires an onboard control loop, operating on ms timescales, to continuously evaluate the success of recently fired electrons after their gyro orbit and to determine the appropriate next firing direction. Since the beam must be fired in the plane perpendicular to B, this also requires determining the instantaneous magnetic field direction from raw onboard field measurements that were taken slightly earlier. The fields' dynamics also require that the guns and detectors must be rapidly, electronically steerable by the control software. The dynamic range and variability of the fields also means that the intensity of the returning beam varies by orders of magnitude due to the ranges of gyro radius and drift step; hence, the current of electrons in the emitted beam (the "beam current") must be adjustable by the onboard control software over a large range.

The dynamics of the ambient plasma electrons, together with the varying intensity of the return beams, provides a third set of challenges. In detecting the return beam, the detector necessarily also detects ambient electrons having a similar energy. For successful operation, the detector must receive sufficient beam electrons to unambiguously recognize a "hit," while rejecting enough of the ambient electrons to prevent them from overwhelming the signal. These two sources of signal place competing requirements on the detector. To maximize the beam signal, the detector must have a large effective area to a mono-energetic, parallel beam, that is, all beam electrons traveling parallel to each other.

That is, it must have a large receiving area for a signal that, in effect, resides at a single point in velocity space. In contrast, to minimize the ambient flux, the detector must limit its geometric factor so that is does not sample too much of the velocity space that is occupied by ambient electrons. Due to varying geometries and beam currents, the instantaneous rate of electrons being detected can at times be extremely large, requiring the detector and its electronics to perform without saturating and to survive over the mission lifetime.

The above challenges imply a fourth set of requirements for onboard control. At the most basic level, the control software must acquire and track the successful firing directions for each of the two gun-detector pairs. It must recognize successful hits and send the associated data to telemetry. These functions must be accomplished in the presence of continually changing ambient conditions and the associated variations in signal to background. To accomplish this task, the onboard software must "navigate" the space of EDI's control parameters.

2. Principle of Technique

The electron-drift technique is based on firing weak beams of electrons as test particles, which are then detected after one or more gyro orbits in the ambient magnetic field (Paschmann et al., 1997, 2001; Quinn et al., 2001). Briefly, as the electrons experience a drift velocity $\boldsymbol{V}_d$, induced by an electric field $\boldsymbol{E}_\perp$, their gyro motion is distorted from circles into cycloids. (A magnetic field gradient also introduces a drift, as discussed at the end of this section.) As the electrons drift, they are displaced in one gyro period T_g by the "drift-step" vector $\boldsymbol{d}$, which is the fundamental quantity measured by EDI.

$$\boldsymbol{d} = \boldsymbol{V}_d T_g. \tag{1}$$

EDI uses two guns and detectors, integrated into a pair of gun-detector units (GDUs), which are mounted on opposite sides of the spacecraft in order to simultaneously sample two gyro orbits. Figure 1 schematically illustrates this with two orbits (not to scale) in the plane perpendicular to $\boldsymbol{B}$, referred to as the $\boldsymbol{B}_\perp$-plane.

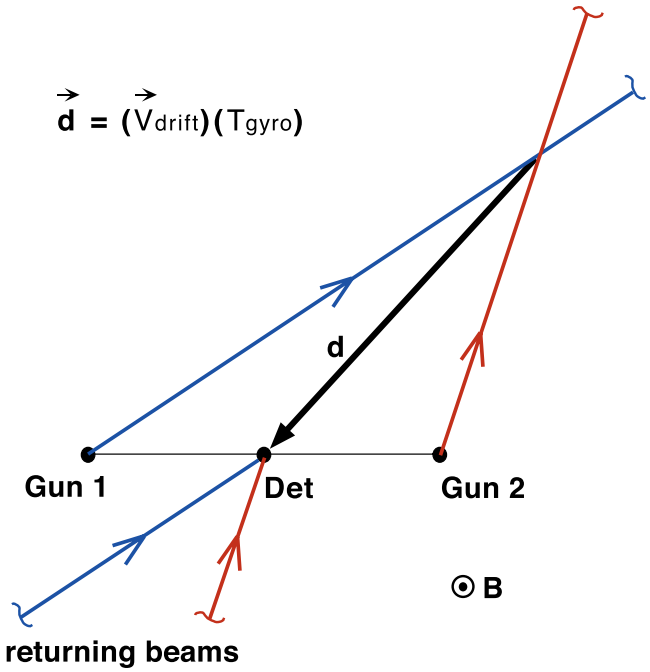

Figure 2. Electron drift instrument triangulation principle, shown projected in the plane perpendicular to $\boldsymbol{B}$. A simplified configuration is shown, with two guns and a single detector, to aid visualization of the triangulation geometry. The "drift step," $\boldsymbol{d}$, is the displacement of the drifting beam electrons in one gyro period. By definition, beams aimed at the tail of the vector $\boldsymbol{d}$ (the Target) return to the detector (the head of $\boldsymbol{d}$) after one gyro orbit. The drift step is measured geometrically, using the firing directions of the two guns and the known positions of the guns and detectors. The beam trajectories appear as straight lines because the gyro radius of the beam electrons is much greater than the scale of the figure. From Quinn et al. (2001).

Given any relative positioning of the two GDUs in the $\boldsymbol{B}_\perp$-plane, there is only one beam firing direction that will return the beam to the opposite detector after a single gyro orbit. Knowing the positions of the two GDUs, together with the firing directions of the guns, is sufficient to determine the drift step, and hence, the drift velocity. This geometric measurement of the drift step, the triangulation technique, is one of two methods used by EDI, the other being time-of-flight, both of which are explained below.

The triangulation technique is illustrated conceptually in Figure 2. In the absence of an electric field (or a magnetic gradient), an electron beam fired in any direction perpendicular to the ambient magnetic field, $\boldsymbol{B}$, returns to its starting point after completing a circular orbit. However, in the presence of a drift, electrons with any firing direction are instead displaced in one gyro period by the drift step. By definition of the drift step, electrons moving through the tail of $\boldsymbol{d}$ hit the detector one gyro period later. Therefore, for the purpose of aiming the electron beams, the tail of $\boldsymbol{d}$ can be viewed as the "Target". According to Equation 1, measurement of the drift step, together with the knowledge of the gyro period, is sufficient to determine the drift velocity.

Figure 2 shows the EDI triangulation principle in simplified form, with two guns and a single "virtual detector" located between them at a distance of one spacecraft diameter from each gun. In reality, the configuration is as shown in Figure 1, with two detectors (co-located with the two guns), but the simplified form is geometrically equivalent because the relative positions between the guns and detector(s) are the same. To display triangulation data, we will use this simplified picture. Figure 2 shows the situation with the beams aimed at the Target, but when aimed in the opposite direction, away from the Target, the electrons will also return to the detector. In practice, the choice of whether electrons are aimed toward or away from the Target is usually determined by gun and detector fields-of-view.

As is evident from Figure 1, the two electron orbits have different lengths, and thus different travel times.

$$T_{1,2} = T_g(1 \pm V_d / V_e), \tag{2}$$

where T_g is the gyro time and V_e is the electron velocity. From Equation 2, it follows immediately that the difference between the two times-of-flight provides a measure of the drift velocity, V_d:

$$\Delta T = T_1 - T_2 = 2(V_d / V_e)T_g = 2(d / V_e), \tag{3}$$

while their sum is twice the gyro time:

$$T_1 + T_2 = 2T_g. \tag{4}$$

Noting that $T_g = 2\pi m_e/eB$, this means that the time-of-flight measurements allow B to be determined as well.

According to Equation 2, the drift introduces a small deviation of the times-of-flight from the gyro time, because the drift velocity is small compared with the velocity of the beam electrons, which is true for the conditions encountered on Cluster. The measurement of the times-of-flight is described in Section 3.

It should be noted that in addition to $\boldsymbol{E} \times \boldsymbol{B}$ motion, the drift of electrons also includes a ∇B component. For the beam energies used by EDI the energy-dependent ∇B drift is typically much smaller than the (energy-independent) $\boldsymbol{E} \times \boldsymbol{B}$ drift. In order to assess, and potentially adjust for, the ∇B drift, EDI is capable of operating with two different beam energies (0.5 and 1.0 keV). After confirming on orbit that the ∇B drift

is so small as to be unimportant in the regimes measured by EDI, Cluster operations routinely used a fixed beam energy.

In summary, it can be stated that the triangulation and time-of-flight techniques complement each other ideally. While the determination of the drift step via triangulation becomes increasingly inaccurate as the Target moves further and further away, as in any triangulation problem, the time-of-flight technique becomes more accurate because, according to Equation 3, ΔT increases with increasing drift steps, and thus, is easier to measure.

3. Implementation and Operational Experience

The EDI instrument consists of two integrated GDUs and a Controller with reprogrammable software, which performs beam acquisition and tracking, receives onboard data from the Flux-Gate Magnetometer (FGM) (Balogh et al., 1997) and Spatio-Temporal Analysis of Field Fluctuations (STAFF) (Cornilleau-Wehrlin et al., 1997) instruments, and produces data for telemetry. A Correlator performs the functions of encoding the outgoing EDI beams, identifying receipt of returning beams by the detectors in the presence of background fluxes of ambient electrons, and performing time-of-flight measurements. Full descriptions of the EDI hardware and beam coding are provided in the study of Paschmann et al. (1997) and Vaith et al. (1998). Briefly, the capabilities of each are as follows.

The gun consists of a conventional electron source with a tungsten filament, followed by an electric octupole deflection system, and emits a weak beam of 0.5 or 1.0 keV electrons, calibrated to fire in any direction within a solid angle of more than a hemisphere. The beam widths are approximately 1° at small deflection angles, increasing to 4° by 1° at large deflections. The emitted beam current is adjustable by the Controller over more than two orders of magnitude (from 1 nA to several hundred nA), and the beam is modulated as described below.

The detector consists of a multi-element, double-focusing optics section and a 128-anode, microchannel plate based, sensor. The detector enables EDI to function across a range of different regimes by having different "Optics States" (i.e., different sets of voltages for the deflection elements within the detector) for various levels of return beam intensity and ambient background flux. Counts from the return beam are determined by the detector's effective area, A, to the mono-energetic and parallel flux, whereas background counts from ambient electrons are set by the detector's geometric factor, G. The Controller's autonomous selection of different States enables adequate signal levels from the beam with respect to the background signal to be maintained by the Controller over a wide range of field strengths and ambient electron fluxes.

The Correlator generates a repetitive digital signal, called a pseudo-noise (PN) code, that is used to on/off-modulate the beam emitted by the gun, and to detect and perform timing of the return beam using delayed versions of the code. A distinctive feature of PN codes is their ideal autocorrelation property, which provides timing of the received signal with much greater resolution than the integration period of its reception. EDI uses two different code sequences, a short one with 15 code elements and a long code with 127 elements. The selection of which code and of the width of the code elements is determined from ambient conditions to maximize accuracy, to avoid aliasing when the code length is substantially shorter than the gyro period, and to differentiate return beams that have gyrated more than once before detection.

To identify return beams in the detected signal, the PN code allows the Correlator to effectively subtract the average background signal of (uncorrelated) ambient electrons, while integrating counts from the correlated beam electrons. Due to counting statistics, this background removal is imperfect and the net result includes a residual noise equal to these statistical fluctuations, that is, approximately equal to the square root of the uncorrelated ambient counts. Therefore, the ratio of signal counts to the square root of the background counts, representing EDI's signal-to-noise, is used to determine beam detection and as a key parameter in the continual onboard adjustments of the operating parameters such as beam current and Optics State.

The Controller acquires successful return beams by sweeping the gun firing direction in the plane perpendicular to $\boldsymbol{B}$ until a beam signal is detected, and then sweeping the beam back and forth for continued "hits," referred to as the "Windshield Wiper Mode." This requires controlling the beam firing and detector look

directions, while adjusting as needed the beam current levels, Optics State, and Correlator parameters. To enable a return beam, the guns must be constantly aimed in the plane perpendicular to the magnetic field to within approximately half the beam width, for which EDI uses the on-board data from FGM and STAFF. The data from FGM are available only every 62.5 ms. To obtain the field at times closer to the beam firing times, EDI integrates the digitized STAFF signals and adds them to the FGM values, taking into account the delay between the FGM measurements and time of receipt by EDI. The flight software is able to work with either FGM data alone or with the combined FGM/STAFF data.

Due to the large geometric factors that can be achieved with suitable choice of the Optics State, the EDI detectors are capable of measuring electron fluxes at very high time resolution. A special purpose "Ambient Mode" exploits this capability, in which the electron guns are turned off, and the ambient electrons are sampled at 0.5 or 1 keV and for example, pitch angles of 0°, 90°, and/or 180°.

Cluster operational experience identified or clarified several areas that were unknown before launch.

- While we had expected to require on-orbit calibration adjustments to the guns to achieve the needed firing accuracy of ≈1° over the full hemisphere, none were needed. Analysis of successful beam hits over months of operation confirmed that the ground calibrations were quite good over the full fields of view.
- Despite immense care in the design of the detector optics, there was uncertainty about the level of sun response with such an open design. In fact, there was no sun-induced background at all.
- The lifetime of the tungsten filaments in the guns posed a concern, but no problems actually occurred.
- The ability to acquire and track return beams was variable, working very well in some regions, that is, in higher magnetic fields, but less so in others. However, concern that the beams would be disrupted before returning proved to be unfounded. Tracking results were poor in very weak magnetic fields and in highly variable fields. (It was always expected that temporal variations happening faster than electron drift instrument (EDI)'s basic 4 ms servo loop, or faster than the gyro period, would be a problem.)
- Prior to launch, it was assumed that measurements would be primarily made using single pairs (one from each gun) of near-simultaneous beams. In practice, the times between hits were too variable for this. Instead, the analysis used accumulated beams over a spin, or sub-spin period (Section 4.1.)

After substantial ground analyses and comparisons with other measurements, we can conclude that EDI does not always provide a measurement, but that when it does the result is highly reliable.

Numerous onboard software patches and table updates, reflecting a substantial learning curve, were required to adjust EDI's control parameters, beam-recognition algorithms, and magnetometer calibrations sufficiently well for the instrument to operate successfully under a wide range of ambient conditions. As the mission progressed, operations were adjusted as follows in response to a variety of conditions.

- In addition to operation in Windshield Wiper (WW) Mode for measuring electric fields, EDI began production of Ambient Mode (AE) data, involving sampling of ambient electron fluxes at selected pitch angles, in April 2004. Switching between WW and AE modes later followed a three-orbit (later six-orbit) cycle.
- It was discovered on orbit that the large beam currents required in weak magnetic field regions, in conjunction with the beam's current modulation, caused interference with the electric wave measurements of the Waves of High Frequency and Sounder for Probing of Electron Density by Relaxation (WHISPER) instrument (Décréau et al., 1997). To reduce this interference, a number of rules for EDI operations were implemented and adjusted over the course of the mission. The rules were a combination of beam current limits and restriction of EDI WW operations to regions of medium to high magnetic fields.
- On Cluster 1, the beam modulation circuit of one gun failed during the commissioning phase, meaning that only full-spin time resolution is available using the single functioning gun. Over time increasing interference by this gun with WHISPER led to suspension of WW operations in July 2010.
- On Cluster 2, WW operation was suspended in April 2004 because interference with WHISPER was more pronounced on that spacecraft.
- On Cluster 3, one of the two guns was decommissioned in July 2010 due to increasing WHISPER interference. WW operations then continued with a single gun until February 2017, when the signal level from the sensor had degraded.

- On both Cluster 1 and Cluster 3, WW operations were resumed, each with a single gun, in 2018 for the purpose of obtaining cross-calibration data. These operations were limited to a ±2 h window around perigee every fourth orbit.
- EDI did not function on Cluster 4 because of a hardware failure at turn-on.
- Use of STAFF data for onboard merging with FGM data was discontinued due to failures of EDI's analog-to-digital converters in September 2003 on Cluster 2 and Cluster 3, and in March 2004 on Cluster 1.

4. Analysis Methods

In every telemetry record (128 ms nominal mode or 16 ms burst mode) EDI transmits the gun firing directions, detector count rates, measured times-of-flight, correlator settings, and information regarding signal quality. Further auxiliary data (beam currents, Optics States, control-loop parameters) are sent in each telemetry format (5.2 s). Because EDI operates asynchronously, time-tags are included in each data record.

With these telemetered data and the Sun Reference Pulse, the automated ground analysis computes the beam directions and gun positions in the spacecraft-sun coordinate system. The standard analysis procedure selects all detected beams within a specified time-interval to determine the drift step. The default analysis interval is one spacecraft spin (4 s), however, shorter intervals can be chosen for higher time resolution (see Quinn et al., 2001). From the telemetry data, the ground software then calculates and outputs the perpendicular drift velocity and the equivalent convection electric field with up to 1 s resolution.

4.1. Triangulation Analysis

The triangulation technique illustrated in Figure 2 implies that the drift step is obtained from the crossing point of a pair of the beams emitted simultaneously by the two guns. It turned out, however, that simultaneous tracking of the Target by both guns is not dependable. We, therefore, use a scheme, where all beams within a certain time interval are combined, as shown in Figure 3. Note that the construction of the drift step from the firing directions of the beams is for a virtual detector location at the center of the spacecraft. Thus, to preserve the correct gun-detector separation distance, the spacecraft is drawn at twice its actual dimensions, and the gun positions, projected into the $\boldsymbol{B}_{\perp}$-plane, lie on the edge of the ellipse as the spacecraft rotates, as explained in Quinn et al. (2001).

The examples in the top part of Figure 3 are for four intervals of 0.5-s duration each, during which time the spacecraft rotates by about 45°, explaining why the multiple hits in each frame are associated with different gun positions and firing directions. An example of the drift step triangulation when single and double runners, that is, electrons having gyrated once or twice, respectively, before returning to the spacecraft, occur simultaneously is shown in the bottom part of Figure 3. The figure emphasizes the importance of the correct identification of the multi-runners, achieved with the help of the time-of-flight measurements.

As an aside, we note that multi-runners are observed because, as described in Section 3, the beam pointing algorithm traverses a range of firing angles in addition to the (a priori unknown) unique direction required to hit the detector after a single gyration. This angular sweeping sometimes includes the firing angles appropriate for multi-runner Targets, in which case they are detected if sufficient signal remains after multiple gyrations. Note that although multi-runner trajectories could, in principle, be precluded by spacecraft blocking on earlier gyrations, in practice they are sometimes, but not always, observed. One expects that the beam "shadow" cast by the spacecraft in the dispersed beam is somewhat filled-in over the subsequent gyro orbit, that is, due to minor deflections from nonuniformities in the ambient magnetic and electric fields.

In order to determine the drift step, the analysis procedure assigns a "cost-function" to candidate Target locations at each grid-point in the $\boldsymbol{B}_{\perp}$-plane. The cost-function is calculated by summing the squared angle-deviations of all beams in the analysis interval from the direction to the candidate grid-point. Analysis intervals of 1, 1/2, or 1/4 spin period may be selected in the standard software. The grid-point with the smallest value of the cost-function is taken as the Target solution. The analysis fails if the drift step and/or the magnetic field significantly vary within the chosen time interval. Such cases can be identified and rejected by the variance in the magnetic field, by the quality of the fit (as measured by its reduced χ^2), and

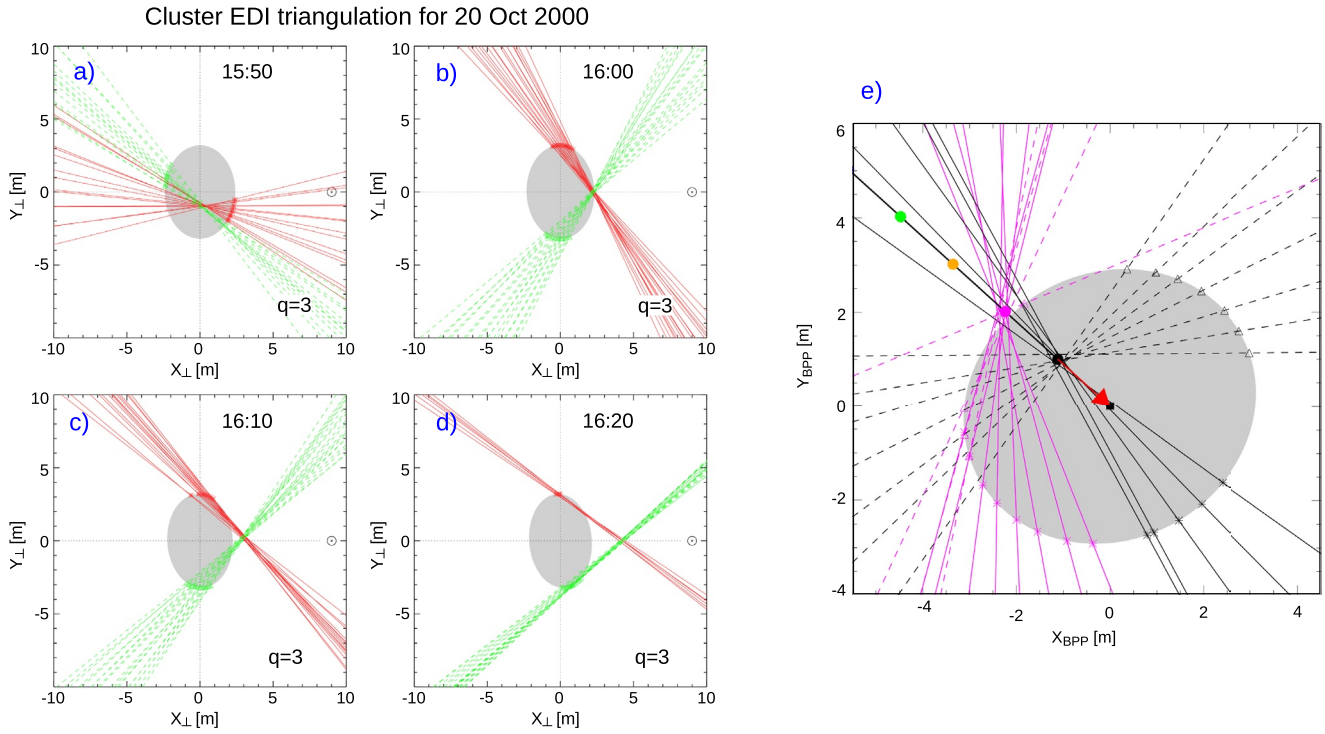

Figure 3. Left: Sample electron drift instrument triangulation plots in the ($X_\perp$, $Y_\perp$) – plane oriented perpendicular to the magnetic field, for four 0.5 s intervals, spaced 10 min apart. Red and green lines are the firing lines of the two electron guns for those times when the beams were properly aimed at the Target and returned to the detectors. The gun positions, projected onto the plane of the figure, move on an ellipse as the spacecraft rotates through 1/8 of a spin in each panel. The measured "drift step" is the vector (not shown) from the beam intersection to the center of the figure (see Quinn et al., 2001). Right: Triangulation plot for a 4-s interval (i.e., one spacecraft spin period), during which there were beams aimed at the Targets for "single-runners" (black lines) and "double-runners" (magenta lines), that is, for electrons having gyrated once or twice, respectively, before returning to the spacecraft. Gun 1 and Gun 2 locations are shown as asterisks and triangles, their firing directions as dashed and solid lines, respectively. The solid circles are placed at the Target locations for single, double, triple, and quadruple runners. In the plot on the right, the axes in the $\boldsymbol{B}_\perp$-plane, although labeled X_{BPP} and Y_{BPP}, are the same as those in the figure on the left (from Paschmann et al., 2001).

by the distribution of the individual beam angle- and magnitude "miss" distances from the computed drift step.

4.2. Time-of-Flight Analysis

The time-of-flight analysis provides three functions. The first and primary purpose is to determine the drift velocity when drift steps are too large for accurate triangulation analysis. Second, it supports triangulation analysis by helping to identify multi-runners, that is, electrons having gyrated more than once. Third, it provides an accurate measurement of B.

It is conceptually straightforward to determine the drift step (and thus, the drift velocity) from the difference in the time-of-flight between the beams directed toward and away from the Target. When the drift step is substantially larger than the spacecraft diameter, the firing directions become nearly parallel. This makes it relatively easy to separate the beams within the analysis interval (e.g., a spin period) into two oppositely directed sets. One set (with the larger times-of-flight) contains beams directed toward the Target, while the other contains beams directed away from the Target. This resolves the ambiguity in the drift direction, while the drift magnitude is then calculated from the difference in the times-of-flight (see Equation 3).

Since the EDI time-of-flight measurements provide a precise determination of the magnetic field magnitude, they have been used routinely to determine the spin-axis offsets of the magnetic field measurements, which are notoriously difficult to assess. The application of EDI data for the FGM calibrations are described

in (Georgescu et al., 2006; Leinweber et al., 2012; Nakamura et al., 2014; Plaschke et al., 2014) and have been applied also on the Mgnetospheric Multiscale mission.

5. Results

In this section, we will review the Cluster results that depended on the use of EDI data. In Section 5.1, we compare the EDI and Electric Field and Waves (EFW) measurements, and in Section 5.2, we discuss results for ion outflows, made possible by combining EDI and EFW data to infer the parallel ion velocity when their energy is so low that they are "hidden" to particle instruments. In Sections 5.3, 5.4, and 5.5, the measurements of plasma convection over the polar cap, magnetotail lobes, and the inner magnetosphere, respectively, are discussed. In Section 5.6, the measurements of ambient electrons are addressed.

5.1. Comparison of EDI With EFW

Cluster carries two types of electric field instruments, the Electric Field and Wave Experiment, EFW (Gustafsson et al., 1997), and EDI, and one of the goals of the Cluster mission was to compare them in various plasma regimes. As discussed in detail in Eriksson et al. (2006), each technique has its merits and weaknesses. Double probe instruments have several relative advantages: Conceptual simplicity, regular sampling at essentially unlimited frequency, the ability to handle rapidly varying fields with arbitrarily large amplitudes, and an operational principle that does not depend on the magnetic field. However, the double probes are sensitive to local effects such as perturbations caused by the spacecraft or by the wire booms that support the probes, and asymmetries in the low energy plasma and photoelectrons that surround the spacecraft, particularly in plasma regimes with low density.

In contrast, the electron drift technique employed by EDI is not sensitive to the spacecraft environment, as the energy of the electrons emitted by EDI, typically 1 keV, is much larger than spacecraft potentials, and for the magnetic fields encountered along the Cluster orbit, the emitted electrons spend most of their time far away from the spacecraft. There is also the fact that EDI measures the full $\boldsymbol{v}_\perp$, equivalent to the full $\boldsymbol{E}_\perp$, while EFW measures only the two components of $\boldsymbol{E}$ in the spin-plane. Another strength of EDI is that the technique is based on simple geometry. Thus, the measurement is reliable when the target tracking is successful; there is no need for offset correction or regime-dependent calibration. On the other hand, EDI necessarily relies upon detecting electrons that return to the spacecraft after one or more gyro-orbits. Therefore, to avoid excessive signal dilution from beam dispersion, the technique requires that the magnetic field be sufficiently strong. Moreover, beam tracking can be adversely affected by rapid variations in the magnetic or electric field, or by sufficiently strong fluxes of natural electrons near the beam energy, which can swamp the beam signal.

Figure 4 presents a comparison of EFW and EDI data, showing agreement to within a fraction of a mV/m during a series of pulsations in the inner magnetosphere. Figure 5 presents a comparison of EFW and EDI data for an interval over the polar cap. As evident from panels (b) and (c), the electric field measurements by EFW and EDI differ by several mV/m during much of this time interval. Evidence that the field seen by EFW is not solely the unperturbed electric field is provided by the agreement between the velocity measurements by EDI and by the Cluster Ion Spectrometry (CIS) Instrument for this interval (see Figure 4 in Eriksson et al., 2006).

An important clue is that the EFW electric field varies with the probe-to-spacecraft potential, shown in the top panel. As potential variations of a few volts do not affect EDI (using electrons of keV energy) this dependence on the spacecraft potential is further evidence that EFW is measuring a perturbed field. The role of the spacecraft potential was further demonstrated for an event in which the spurious field disappeared at the moment the potential control by the Active Spacecraft Potential Control (ASPOC) instrument (Riedler et al., 1997) was turned on (see Figure 13 in Eriksson et al., 2006).

Eriksson et al. (2006) show that the spurious field likely arises from the formation of an ion wake behind the (positively charged) spacecraft when immersed in a supersonic flow. The conclusion that the EFW-EDI discrepancies observed over the polar cap are caused by these spurious fields has been an important contribution by the EDI investigation.

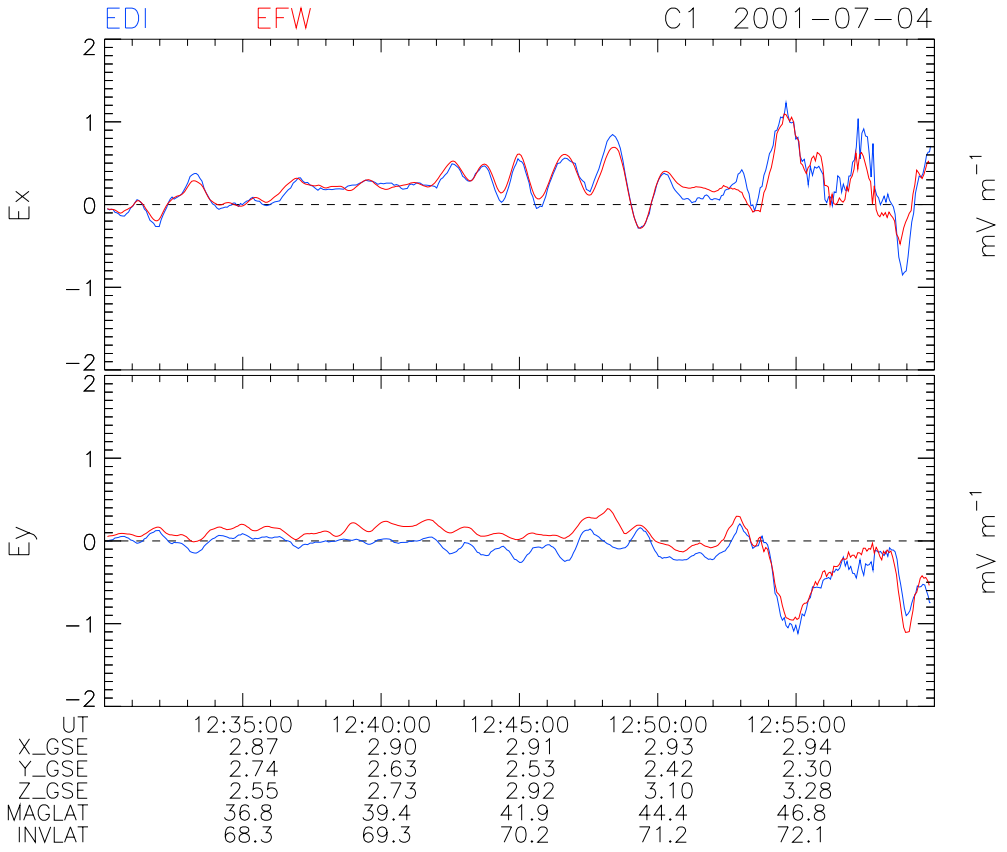

Figure 4. Comparison of electric field and waves (EFW) and electron drift instrument (EDI) data for an interval in the ring current region. The top panel shows the *x*-components, the bottom panel the *y*-components of the electric field. Note that, in contrast to EFW, EDI also measure the *z*-component (not shown). From Eriksson et al. (2006).

5.2. Wake Effects and Ion Outflow

The idea that the spurious electric fields are caused by a wake behind the Cluster spacecraft, directed along the ambient plasma flow velocity, has been exploited by Engwall, Eriksson, André, et al. (2006), Engwall, Eriksson, and Forest (2006), and Engwall et al. (2008, 2009) to estimate the flow velocity of the tenuous, supersonic plasma flow that causes the wake. In their model, illustrated in Figure 6, the double-probe data from EFW and the electron drift velocity data from EDI, combined with a simple model for the wake behind a spacecraft, allow the determination of both the parallel and the perpendicular components, and thus, of the full flow velocity vector, of the ions escaping from the ionosphere and populating the geomagnetic tail lobes.

Little information was available about the outflow of these ions at large distances from Earth because they are normally invisible to spacecraft measurements. The reason is that the potential of a sunlit spacecraft in a tenuous plasma often exceeds the energy-per-charge of the ions, so that the ions cannot reach the instruments onboard the spacecraft. As demonstrated on Cluster by Engwall, Eriksson, André, et al. (2006), cold ions are, however, observed by the CIS instrument if the spacecraft potential is actively controlled by the ASPOC instrument.

Numerous studies have employed the above technique of combining EFW and EDI measurements to study the outflow of cold ions (André et al., 2015; Engwall et al., 2008, 2009; Haaland et al., 2012, 2015; Li et al., 2012, 2013, 2017, 2018; Maes et al., 2017).

In a statistical study, André et al. (2015) have used above technique to determine that the global cold ion outflow is of the order of 10^{26} ions/s, often exceeding the outflow at higher energies. The increasing solar UV flux causes a doubling of the outflow during a solar cycle, due mainly to an increase in density.

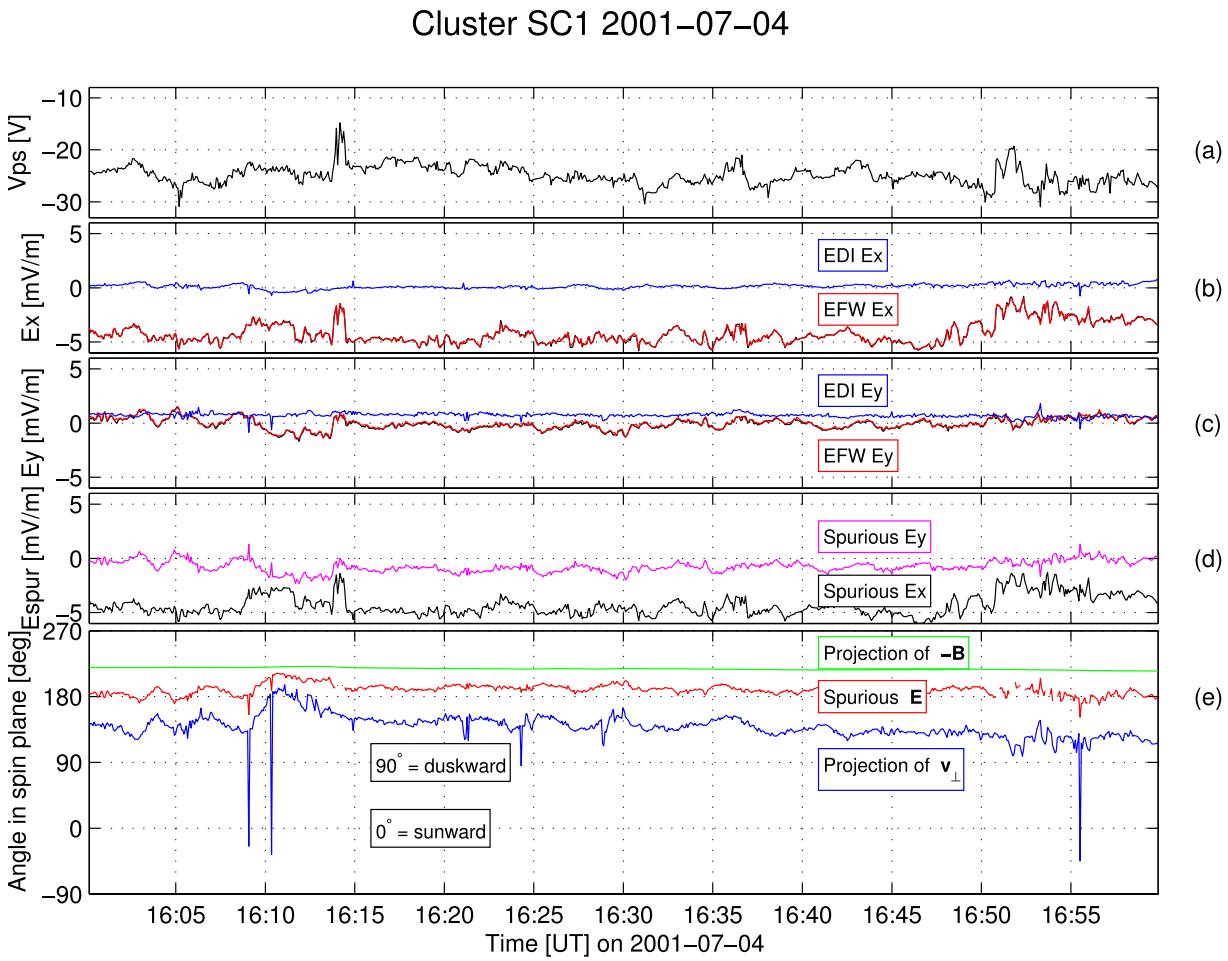

Figure 5. Comparison of electric field and waves (EFW) and electron drift instrument (EDI) data for an interval the exhibits a spurious electric field in the EFW data. The data are for an interval over the polar cap where upwelling ions are observed. From top to bottom, the figure shows: (a) EFW probe-to-spacecraft potential; (b), (c) E_x and E_y, respectively, from EFW (blue) and EDI (red); (d) the X- (black) and Y-components (magenta) of the spurious field, $\boldsymbol{E}_{\rm spur} = \boldsymbol{E}_{\rm EFW} - \boldsymbol{E}_{\rm EDI}$; (e) angle of the projections, into the spacecraft spin plane, of the magnetic field $-\boldsymbol{B}$ (green), the spurious field $\boldsymbol{E}_{\rm spur}$ (red), and the perpendicular velocity $\boldsymbol{V}_\perp$ (blue) from EDI. From Eriksson et al. (2006).

Haaland et al. (2015) studied the total outflow during geomagnetic storms. Their results indicate that outflow rates vary almost an order of magnitude between quiet and very disturbed conditions. The outflow increased to a maximum of 2.7×10^{26}/s during the peak phase of the storm that they investigated. Maes et al. (2017) observed a strong dependence of the ion velocity and density on the solar zenith angle.

Li et al. (2013) have investigated the transport of cold ions between the polar cap ionosphere and the plasma sheet. By combining the EFW and EDI measurements to determine the ion velocities (as discussed in Section 5.1), and the Tsyganenko magnetic field model, they traced the ion motion from the observation site to the plasma sheet. Figures 7a and 7c show the magnetic field lines in the geocentric solar magnetospheric (GSM) (x,z)-plane during quiet and disturbed conditions, respectively, with the red symbols separating the regions, labeled R_a and R_b, where the ions are moving sunward and tailward, respectively. Figures 7b and 7d show the travel times (in seconds) of the ions until they reached the plasma sheet. EDI convection velocity measurements were also used in a recent study by Krcelic et al. (2020) of the escape of oxygen ions measured by the CIS instrument.

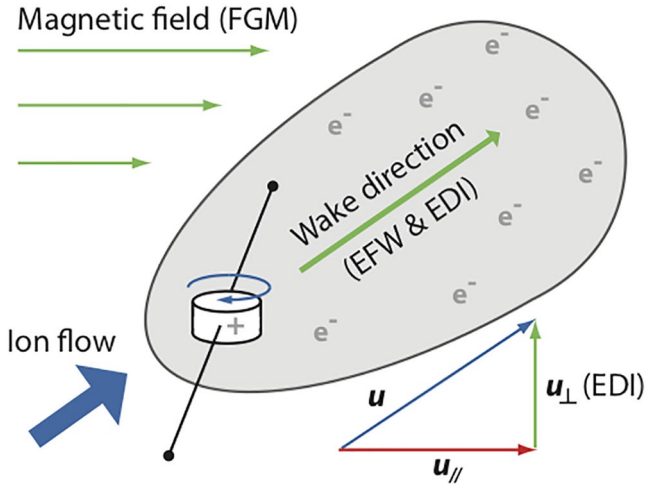

Figure 6. Illustration of the method to derive the flow of cold ions from a combination of electric field and waves and electron drift instrument (EDI) measurements, in the presence of the wake created behind a positively charged spacecraft. With the direction of the flow (green arrow inside the wake) set to the direction of the wake electric field, $\boldsymbol{E}_w = \boldsymbol{E}_{\mathrm{EFW}} - \boldsymbol{E}_{\mathrm{EDI}}$; the direction of the ambient magnetic field, $\boldsymbol{B}$ (green horizontal arrows, from, Flux-Gate Magnetometer (FGM)), and the velocity, $\boldsymbol{u}_\perp$ perpendicular to $\boldsymbol{B}$ (green vertical arrow, from EDI), $\boldsymbol{u}_\parallel$ (red arrow) and then $\boldsymbol{u}$ can be determined. From Engwall et al. (2009).

5.3. Polar Cap Convection

Due to their 90° initial inclination orbits, the Cluster spacecraft cover both polar caps twice per year, allowing detailed studies of the convection patterns. EDI is particularly suited for such studies because it measures the full drift velocity without being affected by spacecraft-induced disturbances.

First results were reported for 20 polar cap passes by Cluster under varying interplanetary magnetic field (IMF; Vaith et al., 2004). They exploited the Cluster multi-point measurements to infer the spatial scales of the convection velocities measured by EDI. The result, shown in Figure 8, is that the scales, when mapping the spacecraft separation distances down to ionospheric altitudes, are always larger than 1 km and sometimes larger than a few hundred km. What is surprising is the observation that poor correlations already occur at separations of only a few tens of km, which is below the resolution achieved by the Super Dual Auroral Radar Network (SuperDARN) radars in their standard scan mode.

Using 6 years of data, Haaland et al. (2007) have derived statistical maps of the polar cap convection. Their study used one-minute averages of the convection measurements, comprising 5,862 h of EDI data, obtained at distances between ∼4 and ∼20 R_E over both hemispheres and sorted according to the clock-angle of the IMF. An improved method (Haaland et al., 2006) to calculate the propagation delay of the IMF was used, and very stringent conditions for the temporal stability of the IMF data were applied.

Figure 9 shows maps of the inferred electric potentials in the northern polar ionosphere, for 8 sectors of the IMF. For strongly southward IMF (Sector 4), the usual two-cell convection pattern is observed, with strong

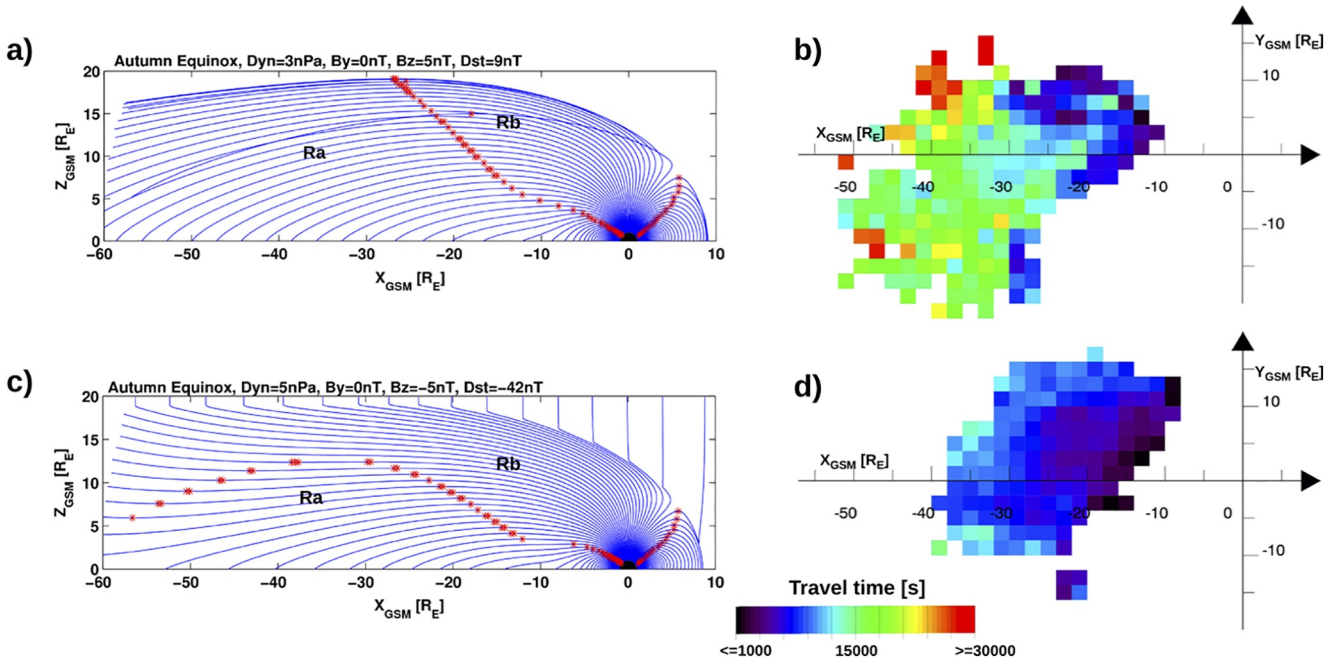

Figure 7. (a) Projection into the geocentric solar magnetospheric (GSM) (x, z)-plane of the magnetic field according to the Tsyganenko T01 magnetic field model for quiet conditions. The red stars mark the separation between earthward convection (labeled R_a) and tailward convection (R_b). (b) Map of the ion transport time from the northern polar cap ionosphere to the plasma sheet during quiet geomagnetic conditions. (c), (d) Same as (a), (b) but for disturbed magnetospheric conditions. From Li et al. (2013).

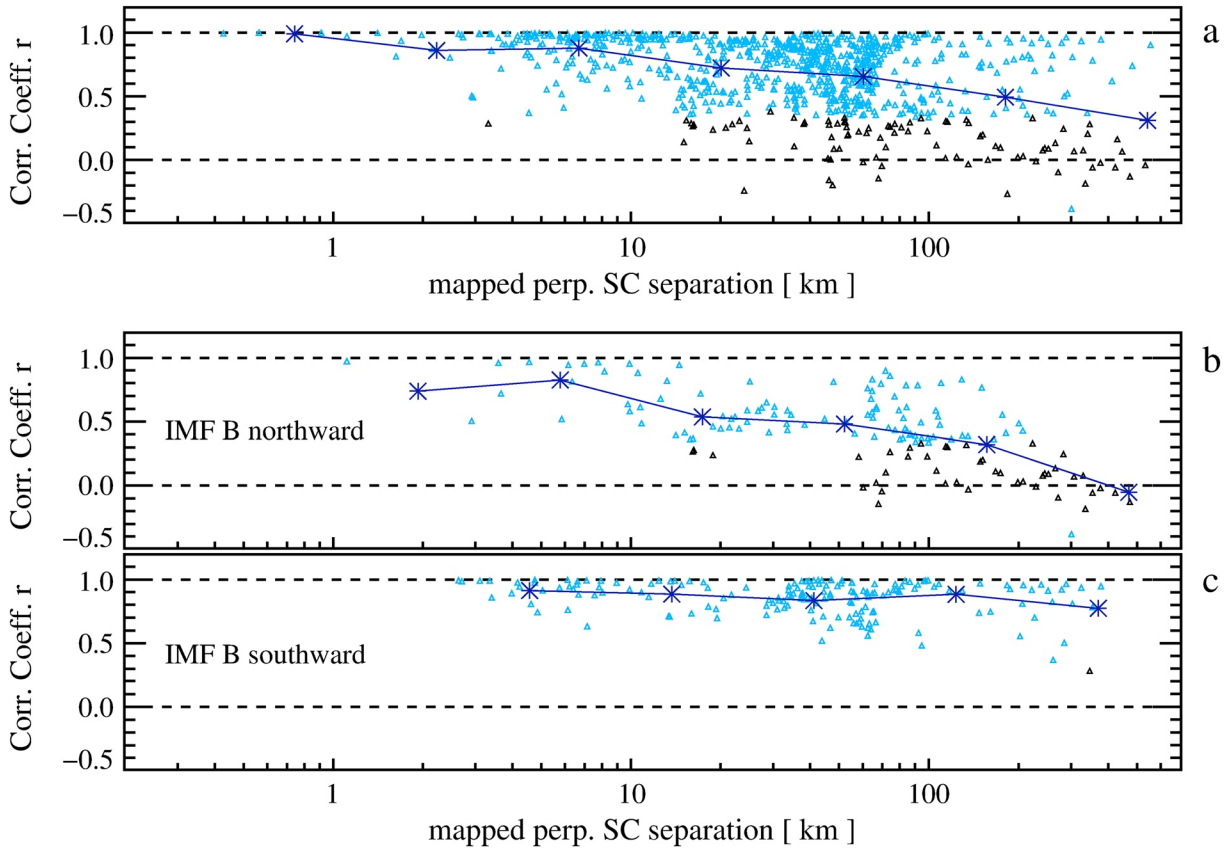

Figure 8. (a) Correlation coefficients of 1-h intervals of 60 s smoothed electron drift instrument convection velocities, scaled to ionospheric altitudes of 100 km, versus spacecraft separation distances transverse to the magnetic field, mapped down to ionospheric altitudes, with the correlation coefficients above and below the significance threshold colored in blue and black, respectively; panels (b) and (c) are the same as (a), except that they apply to the cases for northward and southward interplanetary magnetic field, respectively. The average trend is indicated by the asterisks. From Vaith et al. (2004).

anti-sunward convection over the pole, albeit with significantly skewed cells. The skewing increases in the presence of a positive IMF B_y (Sector 3), as a result of the asymmetrical addition of open flux to the tail lobes. One would expect the skewing to be reversed for a negative IMF B_y (Sector 5), but what is observed is that the flow is nearly anti-sunward over the central polar cap. For sectors centered in the positive or negative *y*-direction (Sectors 2 and 6, respectively), the observations show the emergence of one crescent-shaped and one more rounded cell. What apparently was not previously reported, is that the polar cap potentials are larger for positive B_y (Sector 1) than for negative B_y (Sector 7), and similarly for Sector 2 versus Sector 6, and for Sector 3 versus Sector 5. This is a further illustration of the lack of mirror-symmetry for positive and negative IMF B_y.

Haaland et al. (2007) compared the EDI results with published results based on SuperDARN and low-altitude satellite measurements and found excellent agreement between the convection patterns, particularly the lack of mirror-symmetry between the maps for positive and negative IMF B_y. They emphasized the appearance of a duskward directed flow component for conditions of strongly southward directed IMF, and (c) the general reduction of potentials for northerly IMF directions. A comparison of the northern polar cap potentials showed that the EDI-based values are similar to those from Papitashvili and Rich (2002) and Ruohoniemi and Greenwald (2005), but lower than those of Weimer (2005).

As Haaland et al. (2007) noted, the generally good agreement between the mapped EDI and the ground-based or low-altitude convection measurements shows that the assumption underlying the mapping, namely that magnetic field fields lines are equipotentials, is basically correct They also refer to a study of a single event by Baker et al. (2004) which shows that the amount of consistency between EDI and SuperDARN measurements can be variable.

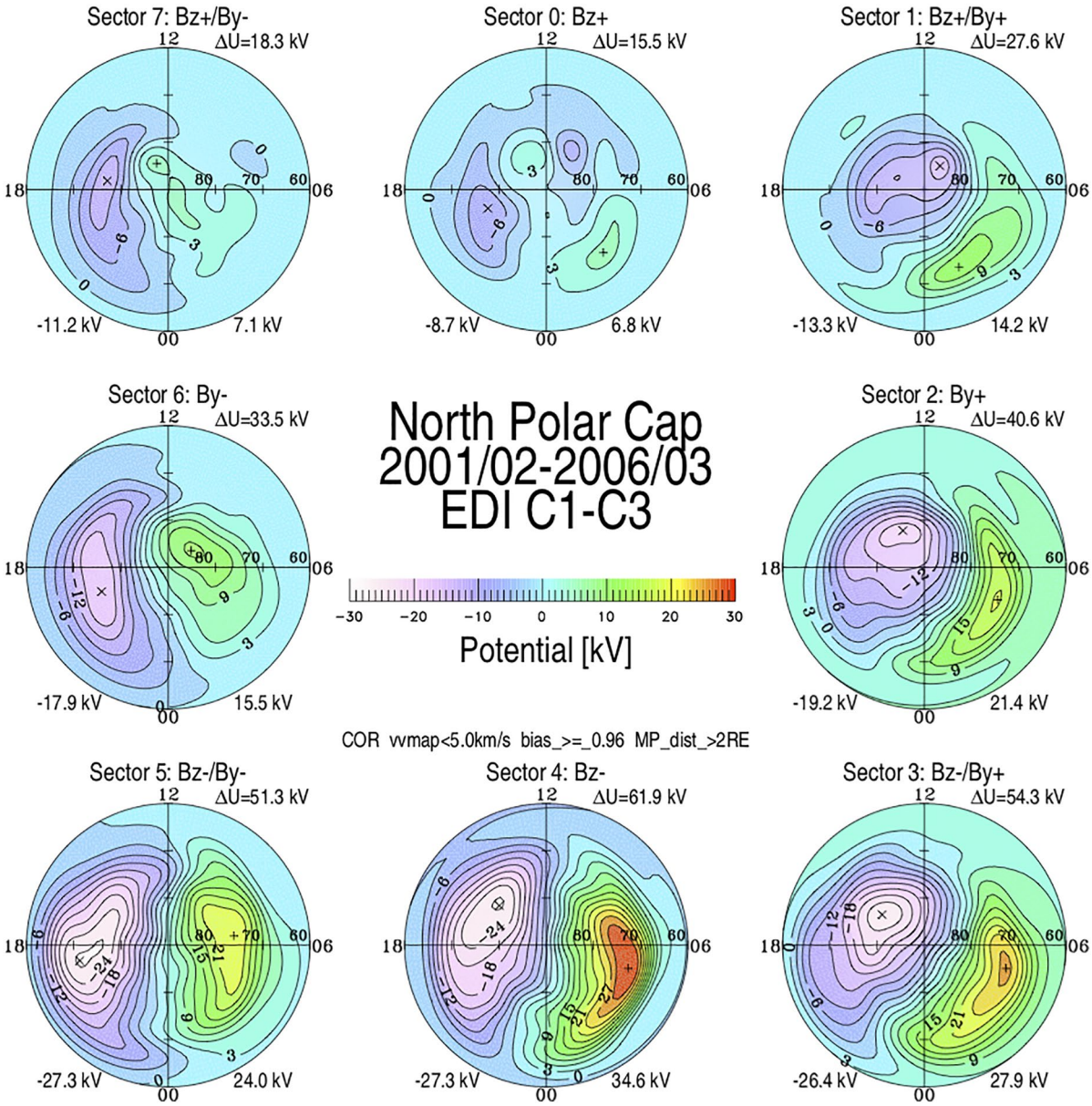

Figure 9. Electric potentials in the northern polar cap, for eight 45°-wide sectors of the interplanetary magnetic field clock-angle, as a function of latitude and magnetic local time, obtained by mapping the electron drift instrument convection velocity measurements into the ionosphere. The background color shows the magnitude of the potential, using the color bar shown at the center. The solid black lines are drawn at fixed values of the potential and are spaced 3 kV apart. The minimum and maximum potentials are listed at the bottom and the total potential at the upper right of each frame. Sectors 0 through 7 are centered at 0°, 45°, 90°, 135°, 180°, 225°, and 270°, respectively. From Haaland et al. (2007).

For northward IMF (Sector 0 in Figure 9), the convection is weak, as indicated by the much larger spacing of the contours. On the nightside, the convection is still anti-sunward, but on the dayside, two more cells appear at high magnetic latitudes. This effect is more prominent in Figure 10, which shows the map for northward IMF, based on a significantly larger database (Förster et al., 2008). The extra cells are often referred to as the lobe-cells. They are created through reconnection, tailward of the polar cusp, of already open polar cap field lines with a strongly northward IMF.

Förster et al. (2007) extended the statistical study by Haaland et al. (2007) by looking at the variances and correlations of the polar cap convection velocities as a function of IMF orientation. Interestingly, the spatial patterns of the variability of the convection as a function of IMF B_y were found to be similar to those of

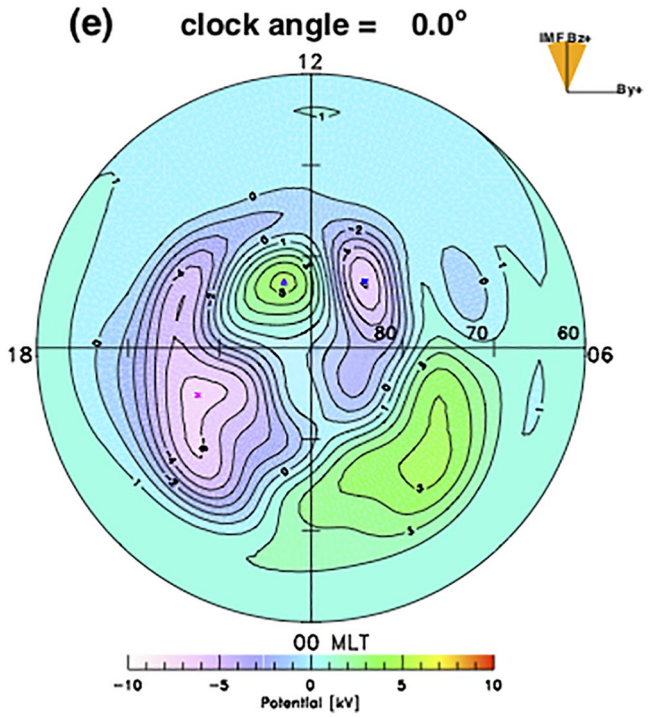

Figure 10. Four-cell potential pattern for a 45° sector centered on 0° clock angle. Note that the contours are spaced 1 kV apart, while the spacing was 3 kV in Figure 9. From Förster et al. (2008).

the convection itself. Correlations with external drivers are in agreement with earlier results (Matsui et al., 2005; Papitashvili & Rich, 2002; Ruohoniemi & Greenwald, 2005). As an example, Figure 11 shows the strong dependence of the polar cap potentials and the convection velocities on the IMF clock angle. Comparisons with a ground-based convection model were reported in Förster et al. (2009). The Interhemispheric differences in ionospheric convection apparent in the EDI observations have been revisited in Förster and Haaland (2015).

EDI convection velocity measurements have also been used to compare with the motion of auroral arcs (Kistler et al., 2002). Figure 12 shows a Keogram, from which the latitudinal motion of auroral features can be inferred. Superimposed on the Keogram are black and white arrows whose slope show the motion of ion outflow structures and the plasma convection velocity measured by the EDI instrument, respectively. A general correspondence between the motion of the aurora and the convective motion of the plasma is observed.

5.4. Lobe Convection

While polar cap convection observations are ubiquitous, Cluster has provided an unprecedented data set of sensitive in situ measurements at large distances. The first EDI measurements in the lobe, at distances between 5 and 15 R_E, covering a limited time period, were published by Noda et al. (2003). They confirmed the expected convection toward the neutral sheet for all IMF conditions, the IMF B_y control of V_y, and a weak convection for northward IMF. A duskward component of the convection velocity for southward IMF was also evident, consistent with the polar cap convection maps (see Section 5.3).

A much larger data set was used for a statistical study of lobe convection by Haaland et al. (2008), consisting of roughly 450,000 one-minute vector measurements of the convection, obtained by EDI between February 2001 and June 2007. For this study, the EDI measurements were mapped from the Cluster location to a YZ_{GSM} plane at $X = -10\,R_E$, basically in the same way as used for the polar cap convection studies discussed in Section 5.3, except that the mapping is to the magnetotail lobes rather than into the polar cap ionosphere, again using the Tsyganenko T2001 magnetic field model (convection patterns are shown in the study).

Because of the mapping along magnetic field lines to the (y, z)-plane at $-10\,R_E$, many of the EDI measurements contributing to the tail-lobe data set were obtained while Cluster was actually located sunward of $-10\,R_E$. In fact only about 20% of the mapped data were actually obtained tailward of $-8\,R_E$, while the remaining 80% were from locations sunward of $-8\,R_E$, including many that were made on the dayside.

Figure 13 shows the two most pronounced correlations. On the left, the dependence of the z-component of the convection velocity on the IMF clock angle, showing the strong dependence expected for reconnection at the dayside magnetopause; and on the right, its dependence on the D_{st} magnetic activity measure, showing the expected increase for more negative D_{st}, that is, for increased tail reconnection. Statistical studies of the convective plasma transport through the Earth's magnetotail lobes for various geomagnetic conditions have been described in Haaland et al. (2009).

In a study by Ohma et al. (2019), the EDI convection data from have been used to investigate how activity in the near-Earth tail affects the average convection pattern in the magnetotail lobes when the IMF is dominated by its B_y component. As shown in Figure 14, the flow becomes more north-south aligned during active periods, which is interpreted as resulting from stronger near-Earth tail reconnection.

EDI convection data for the tail lobes have also been used in the recent studies by Case et al. (2018, 2020).

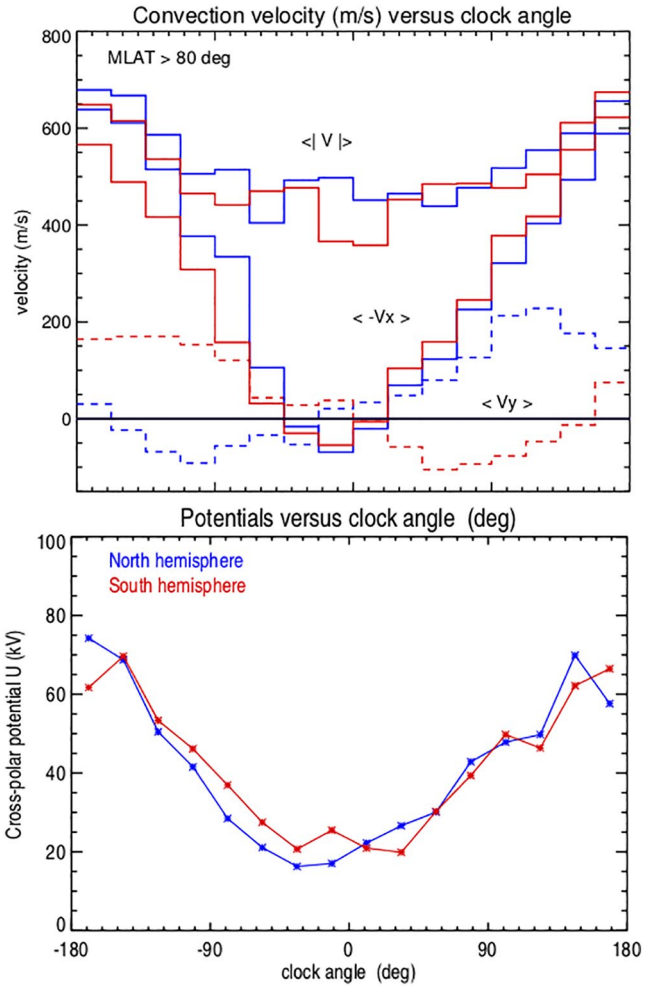

Figure 11. Top: Polar cap potentials as a function of the interplanetary magnetic field clock angle for the Northern (blue) and southern (red) hemisphere. Bottom: Magnitude and components of the convection velocity in m/s. Note that instead of V_x, it is $-V_x$ that is plotted. After Förster et al. (2007).

5.5. Inner Magnetosphere Convection

The relatively low magnitudes of electric fields (of order 1 mV/m or less) and tenuous plasma conditions, combined with the need for knowledge of both components in the (variable) plane perpendicular to B, make systematic measurements with double probes in the equatorial inner magnetosphere quite challenging. In addition to direct measurements, several other techniques have provided key baselines. McIlwain analyzed energy-dependent plasma convection signatures to deduce detailed potential maps (McIlwain, 1972, 1974). Low altitude measurements (which face the uncertainties of mapping to the equatorial region), theoretical models, and simulations have also been important (for references see, e.g., Matsui et al., 2013). An earlier electron beam instrument on ESA's Geos spacecraft obtained results in geosynchronous orbit (Baumjohann & Haerendel, 1985; Baumjohann et al., 1985, 1986).

EDI on Cluster provided an outstanding data set for comprehensive, statistical analyses of convection under a wide variety of conditions. Using the first year of data, Matsui et al. (2003) provided electric field and drift velocity maps for $4 < L < 10$. As more data were acquired, this work was extended to derive detailed electric potential models parameterized by IMF B_y and B_z, D_{st}, K_p, season, and the interplanetary electric field (Matsui et al., 2004, 2005).

To expand the empirical potential model, EDI measurements were augmented with Cluster EFW data, particularly during highly active times when it is difficult for EDI to maintain track, thus providing denser and more continuous sampling (Matsui et al., 2013; Matsui, Puhl-Quinn, et al., 2008; Puhl-Quinn et al., 2008). These works also incorporated data from radar and low altitude satellites to extend the inner boundary of the potential model from $L = 4$ to $L = 2$, and added parameterization by the interplanetary electric field and Kp. Figure 15 (Matsui et al., 2013) shows corotating-frame potential contours derived from the merged data for six K_p ranges. Blue lines indicate the last closed equipotential (LCE) in the inertial frame, while the red line indicates a modeled magnetopause location. In addition to the overall intensification with K_p, two features are immediately apparent: (a) The stagnation point is consistently rotated to later magnetic local time than the dusk meridian, and (b) there is a marked kink in the contours on the nightside in the vicinity of the LCE.

In addition to the above derivations and analyses of the potential electric field, Matsui et al. (2010) analyzed storm-time electric fields, including the non-potential induced components, with an epoch analysis of 71 storms.

Puhl-Quinn et al. (2008) performed a detailed conjugacy analysis of subauroral ion drifts (SAID), using 12 crossings of an SAID channel by Cluster and Defense Meteorological Satellite Program spacecraft in the post-dusk sector to compare measurements at a field-aligned separation of approximately 28,000 km. While the large-scale features of latitudinal width and field-aligned current strength agreed between the ionospheric and magnetospheric measurements, a number of differences highlighted the complexity of magnetosphere-ionosphere coupling at smaller scales.

5.6. Fast Electron Measurements

In its "Ambient Mode," EDI measures natural electrons, at fixed energy and selected pitch angles, with unprecedented time resolution (16 Hz for normal and 128 Hz for burst mode telemetry), by exploiting the unique capability of its two detectors to view in any direction. Ambient Mode data have been used to examine plasma regimes with high temporal variations, such as the magnetic reconnection regions at

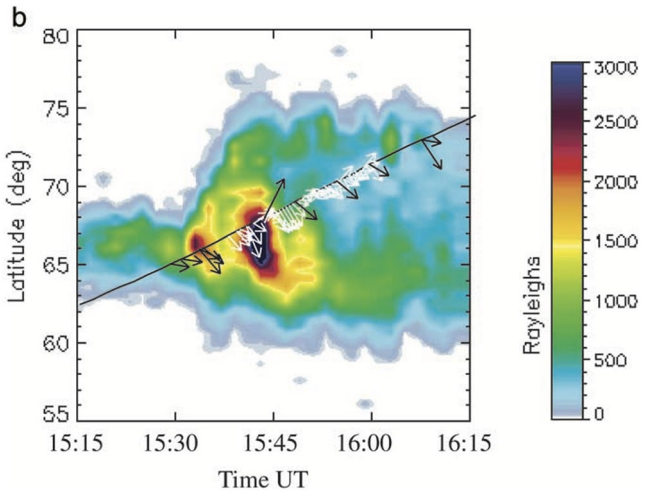

Figure 12. A "Keogram", showing the latitudinal profile of auroral emissions as a function of time at midnight magnetic local time (MLT) from the far ultraviolet camera on the Imager for Magnetopause-to-Aurora mission on January 23, 2001. The black trace shows the track of the Cluster S/C 3. The slope of the black arrows give the velocities of the ion outflow structures, inferred from the time delays between their appearances in the Cluster Ion Spectrometry data on the different Cluster spacecraft. The steeper the slope the larger the northward/southward velocity. The slope of the white arrows give the convection velocities determined from electron drift instrument. From Kistler et al. (2002).

the magnetopause (Mozer et al., 2005) and the neutral sheet (Asano et al., 2006), and at the bow shock (Matsui, Torbert, et al., 2008).

Figure 16 shows one minute of EDI electron and FGM magnetic field data for a partial crossing of the quasi-perpendicular bow shock (Matsui, Torbert, et al., 2008). The large-amplitude oscillations of the electron counts at pitch angles of 10°, 90°, and 170° are in-phase, while the electron counts and the magnetic field magnitude are out of phase. The conclusions were that these oscillations represent mirror mode waves, and that the oscillations of the electron counts in the parallel and anti-parallel directions are related to the oscillation of the parallel electric potential.

6. Summary and Conclusions

EDI is an active experiment in that it measures the displacement that test electrons experience in one (or more) gyrations in the ambient magnetic field under the influence of an electric field. In Section 1, we described the challenges of implementing the simple concept and how these challenges were overcome. The principle of the technique was described in Section 2.

Central to the implementation, described in Section 3, are newly developed gun and detector designs that enable, under the control of EDI's onboard software, the guns and detectors to scan their respective directions of beam firing and detection in the plane perpendicular to the ambient magnetic field and to search for those unique firing directions, determined by the geometry of the fields, that return the beam to the detector. The detector's look direction is slaved to the gun firing direction, so that it can detect the parallel electron beam when it returns, which must be achieved in the presence of both high fluxes of natural electrons and solar UV. The third central element of EDI is the controller and its software, which perform the autonomous control of EDI's operation. This includes the overall beam tracking algorithms and all required lower level actions such as setting the gun and detector deflection voltages, beam currents, type and frequency of the PN code, recognition of beam hits, and generation of telemetry.

As described in Section 4, the drift velocity, and the equivalent electric field, is determined from the beam firing directions and/or from their time-of-flight. The latter has the side effect that it provides a measurement of the magnetic field magnitude and thus can serve, and has indeed served, to determine the spin-axis offsets of the flux-gate magnetometer, FGM, which is notoriously difficult otherwise.

Turning to the science results, one of the most important is based on a unique feature of the Cluster science payload, namely the inclusion of two fundamentally different instruments for measuring the electric field,

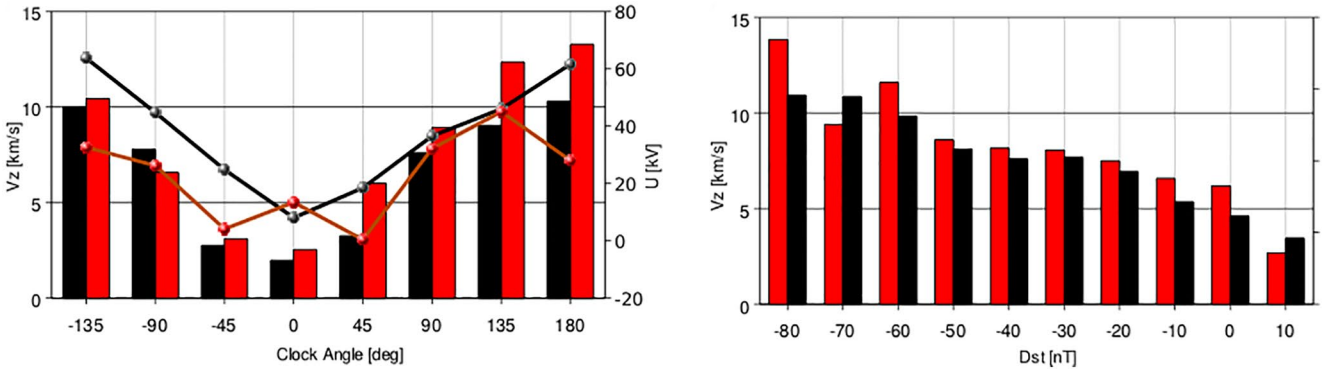

Figure 13. Correlation between the z-component of the tail-lobe convection velocity (in km/s) and interplanetary magnetic field clock angle (left) and the D_{st} index (right). The curves in the left panel show the polar cap potentials. Black (red) color indicates northern (southern) hemisphere. From Haaland et al. (2008).

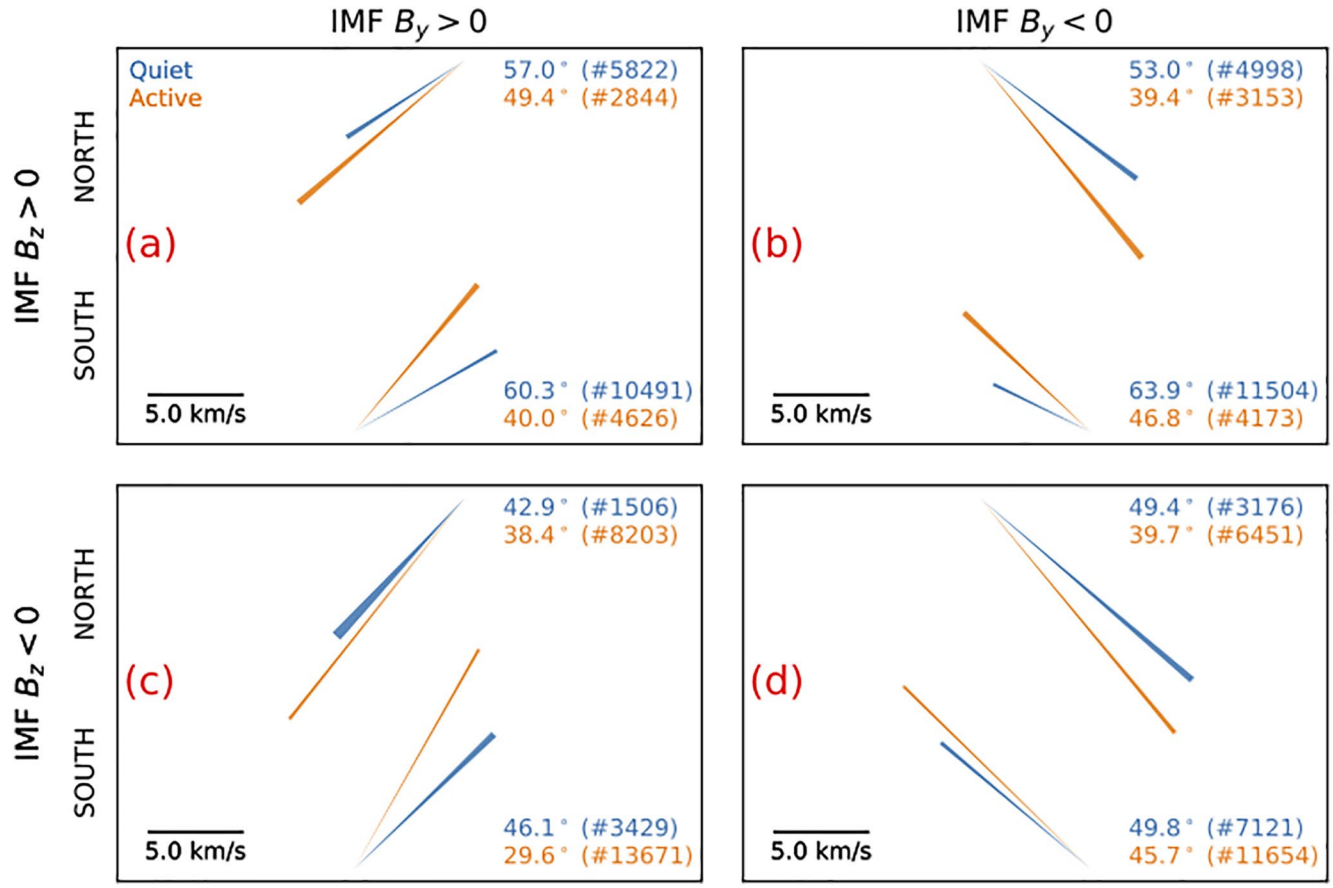

Figure 14. Average convection in the northern and southern central lobes for quiet (blue) and active (orange) conditions, seen from the tail. The averages are taken for two rectangular regions, one in the northern lobe and one in the southern lobe, with $-6\,R_E < Y_{GSM} < 10R_E$ and $8\,R_E < |Z_{GSM}| < 16R_E$. The top two panels are for interplanetary magnetic field (IMF) $B_z > 0$ and positive and negative B_y, respectively; the bottom panels are for IMF $B_z < 0$. The numbers in the upper right of each panel show the angle between each vector and the geocentric solar magnetospheric (GSM) Z-axis, and (in parentheses) the number of data points in each average. The width of the vectors indicates the standard error. From Ohma et al. (2019).

EDI and EFW. Their comparison, dealt with in Section 5.1, established that the two techniques are truly complementary. The double probes of EFW provide measurements at all times and with very high time resolution, but only measure the field in the spacecraft spin plane. However, EFW measurements can be contaminated in conditions of a strong flow and dilute ambient plasma, so that the probes pass through the resulting ion wake. In contrast, the electron-drift technique is unaffected by spacecraft disturbances and measures the full perpendicular electric fields; EDI measurements are reliably accurate when available. However, EDI does not always provide a result, failing when the magnetic field is so low that the gyro radius of the beam electrons becomes very large and consequently the flux of the returning electrons too low, or the magnetic and electric fields are so variable that tracking of the beam target becomes impossible.

A surprising result is that by combining the wake-induced perturbed field measured by EFW and the unperturbed measurements by EDI the wake effect allowed the reconstruction of the flow velocity of the cold ions that are "invisible" to direct measurement by particle detectors. As demonstrated in Section 5.2, many studies exploited this feature to characterize the ion outflow over the polar cap.

EDI's main contribution was that it provided an unprecedented data set of sensitive full-vector measurements for systematic investigation of the plasma convection over the poles and in the inner magnetosphere, and their dependencies on driving parameters such as IMF direction and magnetic activity. Polar measurements mapped to the ionosphere, assuming magnetic field lines are equipotentials, have allowed quantitative comparisons with low altitude and ground measurements, with generally good agreement (see Section 5.3). When mapped out to the magnetotail, as discussed in Section 5.4, they have given a complimentary

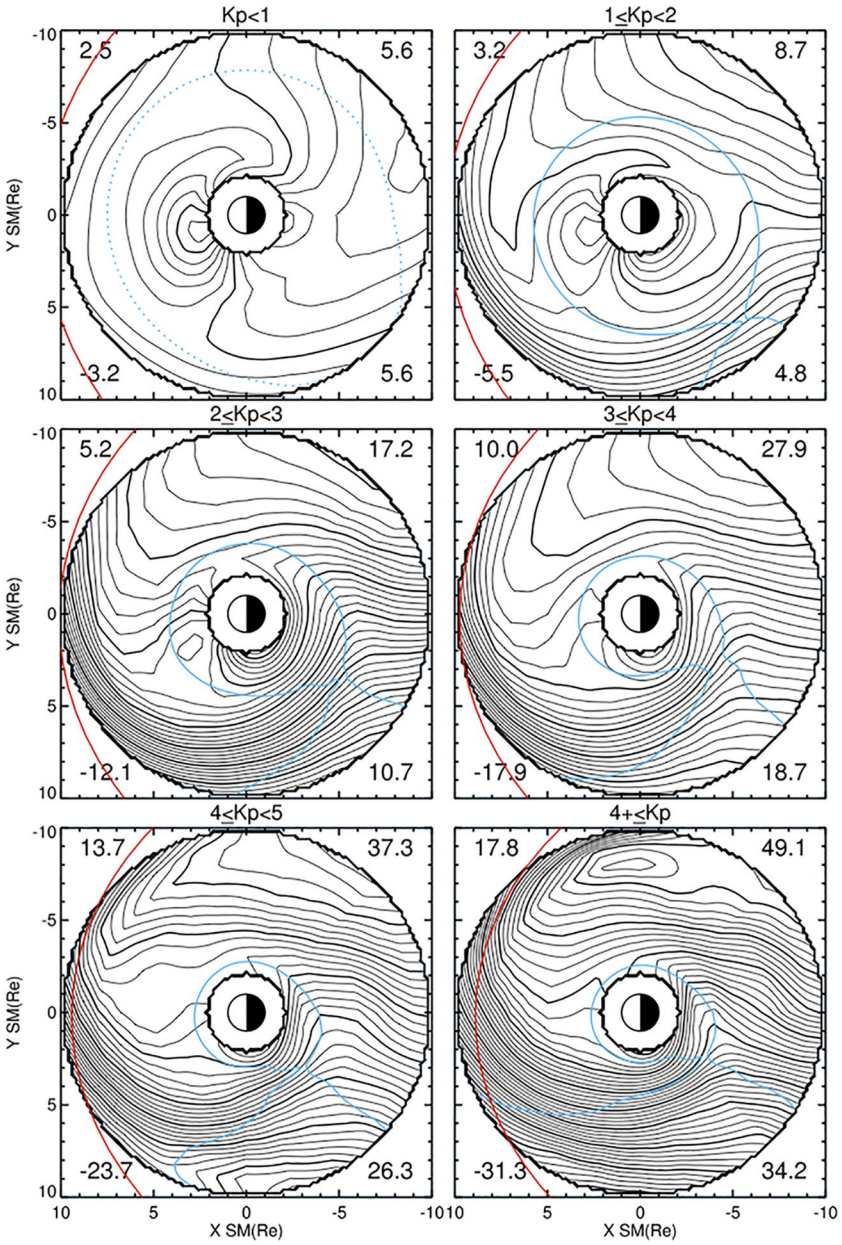

Figure 15. Electric potential contours in the corotating frame for six K_p ranges. For the three lowest K_p ranges the contour intervals are 0.5 kV (thin lines) and 2.5 kV (thick lines). For the upper three K_p ranges those intervals are doubled. Numerical values in the panel corners are: Maximum potential at $L = 2$–10 (top left), minimum potential at $L = 2$–10 (bottom left), potential difference at $L = 2$–10 (top right), and potential difference at $L = 2$–7 (bottom right). From (Matsui et al., 2013).

view of the convection over the full cross-section of the tail. In the inner magnetosphere EDI measurements were used to create a series of empirical potential models, parameterized by external drivers and activity indices, and the model was further expanded by combining EDI and EFW measurements. To support further study of plasma convection in the lobes of the magnetotail, in particular, the skewing of the convection cells for southward IMF and the lack of mirror symmetry in the dependence of the IMF B_y-component, a database with all EDI measurements up to 2020 has been created.

The unique ability of EDI's large geometric-factor detector system to look at any direction over more than 2π steradian, and thus in any direction when the two detectors are combined, allows very high time-resolution

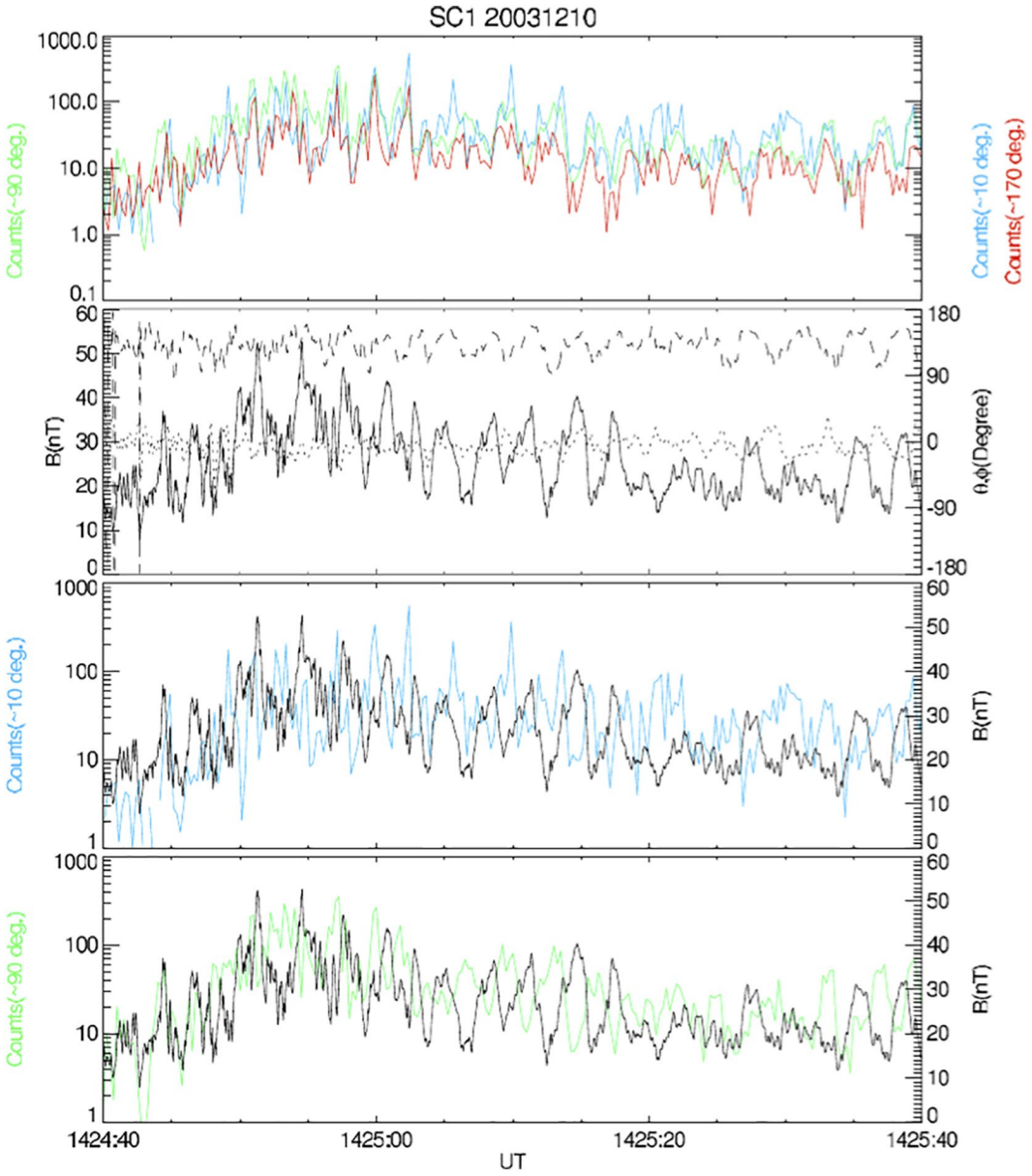

Figure 16. Electron drift instrument electron and Flux-Gate Magnetometer (FGM) magnetic field data for a partial quasi-perpendicular bow shock crossing. The top panel shows electron counts at pitch angles of 10° (blue), 90° (green), and 170° (red). The second panel shows magnetic field magnitude (solid line) and its orientation, in terms of the elevation angle (dotted line) and the azimuth (dashed line), in geocentric solar ecliptic (GSE) coordinates. The third and fourth panels show comparisons of electron counts at 10° (blue) and 90° (green), with magnetic field magnitudes, respectively. From Matsui, Torbert, et al. (2008).

measurements of natural electrons at a specified pitch angle, for example, 0°, 90°, and 180°, albeit at a single energy, as illustrated in Section 5.6. This operational mode, which allows the electron guns to be off, was increasingly utilized during the mission to reduce the interference of the electron beams with the WHISPER instrument.

Data Availability Statement

All Cluster data are available from the Cluster Science Archive at https://www.cosmos.esa.int/web/csa.

Acknowledgments
The authors acknowledge essential contributions to EDI's conceptualization, design, and development by D. Bodet, R. Frenzel, S. Longworth, R. Maheu, F. Melzner, P. Obermayer, P. Parriger, D. Simpson, and C. Young; to its software, data processing, and Cluster operations by A. Allner, B. Briggs, M. Chutter, S. Frey, E. Georgescu (†), G. Leistner, R. Nakamura, U. Pagel, P. Puhl-Quinn, and M. Schmidt; and scientists who contributed to turning EDI's concept to reality, O. Bauer (†), T. Bauer, W. Fillius, K. Lynch, and E. Whipple (†). The authors gratefully acknowledge the profound contributions to EDI and Cluster by N. Sckopke (†), whose scientific and personal presence is greatly missed. G. Paschmann and J. M. Quinn deeply appreciate the technical inspirations, creative leadership, and long friendship of Ed Shelley, who left us this year.

References

André, M., Li, K., & Eriksson, A. I. (2015). Outflow of low-energy ions and the solar cycle. *Journal of Geophysical Research: Space Physics*, *120*(2), 1072–1085. https://doi.org/10.1002/2014JA020714

Asano, Y., Nakamura, R., Runov, A., Baumjohann, W., McIlwain, C., Paschmann, G., et al. (2006). Detailed analysis of low-energy electron streaming in the near-Earth neutral line region during a substorm. *Advances in Space Research*, *37*(7), 1382–1387. https://doi.org/10.1016/j.asr.2005.05.059

Baker, J. B. H., Greenwald, R. A., Ruohoniemi, J. M., Förster, M., Paschmann, G., Donovan, E. F., & Balogh, A. (2004). Conjugate comparison of Super Dual Auroral Radar Network and Cluster electron drift instrument measurements of $E \times B$ plasma drift. *Journal of Geophysical Research*, *109*(A1), A01209. https://doi.org/10.1029/2003JA009912

Balogh, A., Dunlop, M. W., Cowley, S. W. H., Southwood, D. J., Thomlinson, J. G., Glassmeier, K. H., et al. (1997). The cluster magnetic field investigation. *Space Science Reviews*, *79*, 65–91. https://doi.org/10.1007/978-94-011-5666-0_3

Baumjohann, W., & Haerendel, G. (1985). Magnetospheric convection observed between 0600 and 2100 LT: Solar wind and IMF dependence. *Journal of Geophysical Research*, *90*(A7), 6370–6378. https://doi.org/10.1029/JA090iA07p06370

Baumjohann, W., Haerendel, G., & Melzner, F. (1985). Magnetospheric convection observed between 0600 and 2100 LT: Variations with Kp. *Journal of Geophysical Research*, *90*(A1), 393–398. https://doi.org/10.1029/JA090iA01p00393

Baumjohann, W., Nakamura, R., & Haerendel, G. (1986). Dayside equatorial-plane convection and IMF sector structure. *Journal of Geophysical Research*, *91*(A4), 4557–4560. https://doi.org/10.1029/JA091iA04p04557

Case, N. A., Grocott, A., Fear, R. C., Haaland, S., & Lane, J. H. (2020). Convection in the magnetosphere-ionosphere system: A multimission survey of its response to IMF ¡span type="mathematics"¿B_y reversals. *Journal of Geophysical Research: Space Physics*, *125*(10), e27541. https://doi.org/10.1029/2019JA027541

Case, N. A., Grocott, A., Haaland, S., Martin, C. J., & Nagai, T. (2018). Response of Earth's neutral sheet to reversals in the IMF B_y component. *Journal of Geophysical Research: Space Physics*, *123*(10), 8206–8218. https://doi.org/10.1029/2018JA025712

Cornilleau-Wehrlin, N., Chauveau, P., Louis, S., Meyer, A., Nappa, J. M., Perraut, S., et al. (1997). The cluster spatio-temporal analysis of field fluctuations (STAFF) experiment. *Space Science Reviews*, *79*, 107–136. https://doi.org/10.1023/A:1004979209565

Décréau, P. M. E., Fergeau, P., Krannosels'kikh, V., Leveque, M., Martin, P., Randriamboarison, O., et al. (1997). Whisper, a resonance sounder and wave analyzer: Performances and perspectives for the cluster mission. *Space Science Reviews*, *79*, 157–193. https://doi.org/10.1023/A:1004931326404

Engwall, E., Eriksson, A. I., André, M., Dandouras, I., Paschmann, G., Quinn, J., & Torkar, K. (2006). Low-energy (order 10 eV) ion flow in the magnetotail lobes inferred from spacecraft wake observations. *Geophysical Research Letters*, *33*(6), L06110. https://doi.org/10.1029/2005GL025179

Engwall, E., Eriksson, A. I., Cully, C. M., André, M., Puhl-Quinn, P. A., Vaith, H., & Torbert, R. (2009). Survey of cold ionospheric outflows in the magnetotail. *Annales Geophysicae*, *27*(8), 3185–3201. https://doi.org/10.5194/angeo-27-3185-2009

Engwall, E., Eriksson, A. I., Cully, C. M., André, M., Torbert, R., & Vaith, H. (2008). Earth's ionospheric outflow dominated by hidden cold plasma. *Nature Geoscience*, *2*, 24–27. https://doi.org/10.1038/ngeo387

Engwall, E., Eriksson, A. I., & Forest, J. (2006). Wake formation behind positively charged spacecraft in flowing tenuous plasmas. *Physics of Plasmas*, *13*(6), 062904. https://doi.org/10.1063/1.2199207

Eriksson, A. I., André, M., Klecker, B., Laakso, H., Lindqvist, P.-A., Mozer, F., et al. (2006). Electric field measurements on cluster: Comparing the double-probe and electron drift techniques. *Annales Geophysicae*, *24*(1), 275–289. https://doi.org/10.5194/angeo-24-275-2006

Förster, M., Feldstein, Y. I., Haaland, S. E., Dremukhina, L. A., Gromova, L. I., & Levitin, A. E. (2009). Magnetospheric convection from cluster EDI measurements compared with the ground-based ionospheric convection model IZMEM. *Annales Geophysicae*, *27*(8), 3077–3087. https://doi.org/10.5194/angeo-27-3077-2009

Förster, M., & Haaland, S. (2015). Interhemispheric differences in ionospheric convection: Cluster EDI observations revisited. *Journal of Geophysical Research: Space Physics*, *120*(7), 5805–5823. https://doi.org/10.1002/2014JA020774

Förster, M., Haaland, S. E., Paschmann, G., Quinn, J. M., Torbert, R. B., Vaith, H., & Kletzing, C. A. (2008). High-latitude plasma convection during northward IMF as derived from in-situ magnetospheric cluster EDI measurements. *Annales Geophysicae*, *26*(9), 2685–2700. https://doi.org/10.5194/angeo-26-2685-2008

Förster, M., Paschmann, G., Haaland, S. E., Quinn, J. M., Torbert, R. B., Vaith, H., & Kletzing, C. A. (2007). High-latitude plasma convection from cluster EDI: Variances and solar wind correlations. *Annales Geophysicae*, *25*(7), 1691–1707. https://doi.org/10.5194/angeo-25-1691-2007

Georgescu, E., Vaith, H., Fornacon, K.-H., Auster, U., Balogh, A., Carr, C., & Torbert, R. (2006). Use of EDI time-of-flight data for FGM calibration check on cluster. In *Cluster and double star symposium*. ESTEC.

Gustafsson, G., Bostrom, R., Holback, B., Holmgren, G., Lundgren, A., Stasiewicz, K., et al. (1997). The electric field and wave experiment for the cluster mission. *Space Science Reviews*, *79*, 137–156. https://doi.org/10.1007/978-94-011-5666-0_6

Haaland, S., Eriksson, A., André, M., Maes, L., Baddeley, L., Barakat, A., et al. (2015). Estimation of cold plasma outflow during geomagnetic storms. *Journal of Geophysical Research: Space Physics*, *120*(12), 10622–10639. https://doi.org/10.1002/2015JA021810

Haaland, S., Eriksson, A., Engwall, E., Lybekk, B., Nilsson, H., Pedersen, A., et al. (2012). Estimating the capture and loss of cold plasma from ionospheric outflow. *Journal of Geophysical Research*, *117*(A7), A07311. https://doi.org/10.1029/2012JA017679

Haaland, S., Lybekk, B., Svenes, K., Pedersen, A., Förster, M., Vaith, H., & Torbert, R. (2009). Plasma transport in the magnetotail lobes. *Annales Geophysicae*, *27*(9), 3577–3590. https://doi.org/10.5194/angeo-27-3577-2009

Haaland, S., Paschmann, G., Förster, M., Quinn, J., Torbert, R., McIlwain, C. E., et al. (2007). High-latitude plasma convection from cluster EDI measurements: Method and IMF-dependence. *Annales Geophysicae*, *25*(1), 239–253. https://doi.org/10.5194/angeo-25-239-2007

Haaland, S., Paschmann, G., Förster, M., Quinn, J., Torbert, R., Vaith, H., et al. (2008). Plasma convection in the magnetotail lobes: Statistical results from cluster EDI measurements. *Annales Geophysicae*, *26*(8), 2371–2382. https://doi.org/10.5194/angeo-26-2371-2008

Haaland, S., Paschmann, G., & Sonnerup, B. U. Ã. (2006). Comment on "A new interpretation of Weimer et al.'s solar wind propagation delay technique" by Bargatze et al. *Journal of Geophysical Research*, *111*(A6), A06102. https://doi.org/10.1029/2005JA011376

Kistler, L. M., Frey, H. U., Möbius, E., Mouikis, C., Quinn, J. M., Klecker, B., et al. (2002). Motion of auroral ion outflow structures observed with CLUSTER and IMAGE FUV. *Journal of Geophysical Research*, *107*(A8), 1186–1191. https://doi.org/10.1029/2001JA005075

Krcelic, P., Haaland, S., Maes, L., Slapak, R., & Schillings, A. (2020). Estimating the fate of oxygen ion outflow from the high-altitude cusp. *Annales Geophysicae*, *38*(2), 491–505. https://doi.org/10.5194/angeo-38-491-2020

Leinweber, H. K., Russell, C. T., & Torkar, K. (2012). In-flight calibration of the spin axis offset of a fluxgate magnetometer with an electron drift instrument. *Measurement Science and Technology*, *23*, 105003. https://doi.org/10.1088/0957-0233/23/10/105003

Li, K., Haaland, S., Eriksson, A., André, M., Engwall, E., Wei, Y., et al. (2012). On the ionospheric source region of cold ion outflow. *Geophysical Research Letters*, *39*(18), L18102. https://doi.org/10.1029/2012GL053297

Li, K., Haaland, S., Eriksson, A., André, M., Engwall, E., Wei, Y., et al. (2013). Transport of cold ions from the polar ionosphere to the plasma sheet. *Journal of Geophysical Research: Space Physics*, *118*(9), 5467–5477. https://doi.org/10.1002/jgra.50518

Li, K., Wei, Y., André, M., Eriksson, A., Haaland, S., Kronberg, E. A., et al. (2017). Cold ion outflow modulated by the solar wind energy input and tilt of the geomagnetic dipole. *Journal of Geophysical Research: Space Physics*, *122*(10), 10658–10668. https://doi.org/10.1002/2017JA024642

Li, K., Wei, Y., Haaland, S., Kronberg, E. A., Rong, Z. J., Maes, L., et al. (2018). Estimating the kinetic energy budget of the polar wind outflow. *Journal of Geophysical Research: Space Physics*, *123*(9), 7917–7929. https://doi.org/10.1029/2018JA025819

Maes, L., Maggiolo, R., DeÂ Keyser, J., André, M., Eriksson, A. I., Haaland, S., et al. (2017). Solar illumination control of the polar wind. *Journal of Geophysical Research: Space Physics*, *122*(11), 11468–11480. https://doi.org/10.1002/2017JA024615

Matsui, H., Jordanova, V. K., Quinn, J. M., Torbert, R. B., & Paschmann, G. (2004). Derivation of electric potential patterns in the inner magnetosphere from Cluster EDI data: Initial results. *Journal of Geophysical Research*, *109*(A10), A10202. https://doi.org/10.1029/2003JA010319

Matsui, H., Puhl-Quinn, P. A., Bonnell, J. W., Farrugia, C. J., Jordanova, V. K., Khotyaintsev, Y. V., et al. (2010). Characteristics of storm time electric fields in the inner magnetosphere derived from cluster data. *Journal of Geophysical Research*, *115*(A11), A11215. https://doi.org/10.1029/2010JA015450

Matsui, H., Puhl-Quinn, P. A., Jordanova, V. K., Khotyaintsev, Y., Lindqvist, P.-A., & Torbert, R. B. (2008). Derivation of inner magnetospheric electric field (UNH-IMEF) model using cluster data set. *Annales Geophysicae*, *26*(9), 2887–2898. https://doi.org/10.5194/angeo-26-2887-2008

Matsui, H., Quinn, J. M., Torbert, R. B., Jordanova, V. K., Baumjohann, W., Puhl-Quinn, P. A., & Paschmann, G. (2003). Electric field measurements in the inner magnetosphere by Cluster EDI. *Journal of Geophysical Research*, *108*(A9), 1352. https://doi.org/10.1029/2003JA009913

Matsui, H., Quinn, J. M., Torbert, R. B., Jordanova, V. K., Puhl-Quinn, P. A., & Paschmann, G. (2005). IMF By and the seasonal dependencies of the electric field in the inner magnetosphere. *Annales Geophysicae*, *23*, 2671–2678. https://doi.org/10.5194/angeo-23-2671-2005

Matsui, H., Torbert, R. B., Baumjohann, W., Kucharek, H., Schwartz, S. J., Mouikis, C. G., et al. (2008). Oscillation of electron counts at 500 eV downstream of the quasi-perpendicular bow shock. *Journal of Geophysical Research*, *113*(A8), A08223. https://doi.org/10.1029/2007JA012939

Matsui, H., Torbert, R. B., Spence, H. E., Khotyaintsev, Y. V., & Lindqvist, P. A. (2013). Revision of empirical electric field modeling in the inner magnetosphere using Cluster data. *Journal of Geophysical Research: Space Physics*, *118*(7), 4119–4134. https://doi.org/10.1002/jgra.50373

McIlwain, C. E. (1972). Plasma Convections in the Vicinity of the Geosynchronous Orbit. In B. M. McCormac (Ed.), Earth's Magnetospheric Processes (Vol. 32, pp. 268–279). https://doi.org/10.1007/978-94-010-2896-7_25

McIlwain, C. E. (1974). Substorm injection boundaries. In B. M. McCormac (Ed.), Magnetospheric physics (Vol. 44, p. 387). https://doi.org/10.1007/978-94-010-2214-9_12

Melzner, F., Metzner, G., & Antrack, D. (1978). The GEOS electron beam experiment S329. *Space Science Instrumentation*, *4*, 45–55.

Mozer, F. S., Bale, S. D., McFadden, J. P., & Torbert, R. B. (2005). New features of electron diffusion regions observed at subsolar magnetic field reconnection sites. *Geophysical Research Letters*, *32*(24), L24102. https://doi.org/10.1029/2005GL024092

Nakamura, R., Plaschke, F., Teubenbacher, R., Giner, L., Baumjohann, W., Magnes, W., et al. (2014). Interinstrument calibration using magnetic field data from the flux-gate magnetometer (FGM) and electron drift instrument (EDI) onboard Cluster. *Geoscientific Instrumentation, Methods and Data Systems*, *3*, 1–11. https://doi.org/10.5194/gi-3-1-2014

Noda, H., Baumjohann, W., Nakamura, R., Torkar, K., Paschmann, G., Vaith, H., & Quinn, J. M. (2003). Tail lobe convection observed by Cluster/EDI. *Journal of Geophysical Research*, *108*(A7), 1288. https://doi.org/10.1029/2002JA009669

Ohma, A., Østgaard, N., Reistad, J. P., Tenfjord, P., Laundal, K. M., Moretto Jørgensen, T., et al. (2019). Observations of asymmetric lobe convection for weak and strong tail activity. *Journal of Geophysical Research: Space Physics*, *124*(12), 9999–10017. https://doi.org/10.1029/2019JA026773

Papitashvili, V. O., & Rich, F. J. (2002). High-latitude ionospheric convection models derived from Defense Meteorological Satellite Program ion drift observations and parameterized by the interplanetary magnetic field strength and direction. *Journal of Geophysical Research*, *107*(A8), 1198–1201. https://doi.org/10.1029/2001JA000264

Paschmann, G., Melzner, F., Frenzel, R., Vaith, H., Parigger, P., Pagel, U., et al. (1997). The Electron Drift Instrument for Cluster. *Space Science Reviews*, *79*, 233–269. https://doi.org/10.1023/a:1004917512774

Paschmann, G., Quinn, J. M., Torbert, R. B., Vaith, H., McIlwain, C. E., Haerendel, G., et al. (2001). The Electron Drift Instrument on Cluster: Overview of first results. *Annales Geophysicae*, *19*, 1273–1288. https://doi.org/10.5194/angeo-19-1273-2001

Plaschke, F., Nakamura, R., Leinweber, H. K., Chutter, M., Vaith, H., Baumjohann, W., et al. (2014). Flux-gate magnetometer spin axis offset calibration using the electron drift instrument. *Measurement Science and Technology*, *25*(10), 105008. https://doi.org/10.1088/0957-0233/25/10/105008

Puhl-Quinn, P. A., Matsui, H., Jordanova, V. K., Khotyaintsev, Y., & Lindqvist, P. A. (2008). An effort to derive an empirically based, inner-magnetospheric electric field model: Merging Cluster EDI and EFW data. *Journal of Atmospheric and Solar-Terrestrial Physics*, *70*(2–4), 564–573. https://doi.org/10.1016/j.jastp.2007.08.069

Quinn, J. M., Paschmann, G., Torbert, R. B., Vaith, H., McIlwain, C. E., Haerendel, G., et al. (2001). Cluster EDI convection measurements across the high-latitude plasma sheet boundary at midnight. *Annales Geophysicae*, *19*, 1669–1681. https://doi.org/10.5194/angeo-19-1669-2001

Riedler, W., Torkar, K., Rudenauer, F., Fehringer, M., Pedersen, A., Schmidt, R., et al. (1997). Active spacecraft potential control. *Space Science Reviews*, *79*, 271–302. https://doi.org/10.1023/A:1004921614592

Ruohoniemi, J. M., & Greenwald, R. A. (2005). Dependencies of high-latitude plasma convection: Consideration of interplanetary magnetic field, seasonal, and universal time factors in statistical patterns. *Journal of Geophysical Research*, *110*(A9), A09204. https://doi.org/10.1029/2004JA010815

Vaith, H., Frenzel, R., Paschmann, G., & Melzner, E. (1998). Electron gyro time measurement technique for determining electric and magnetic fields. In Washington DC American Geophysical Union Geophysical Monograph Series (Vol. 103, pp. 47–52). https://doi.org/10.1029/GM103p0047

Vaith, H., Paschmann, G., Quinn, J. M., Förster, M., Georgescu, E., Haaland, S. E., et al. (2004). Plasma convection across the polar cap, plasma mantle and cusp: Cluster EDI observations. *Annales Geophysicae*, *22*(7), 2451–2461. https://doi.org/10.5194/angeo-22-2451-2004

Weimer, D. R. (2005). Predicting surface geomagnetic variations using ionospheric electrodynamic models. *Journal of Geophysical Research*, *110*(A12), A12307. https://doi.org/10.1029/2005JA011270